Dissecting PADI6 function defines oocyte cytoplasmic lattices as regulatory hubs for fundamental cellular processes

Authors

Jack P. C. Williams[1,2], Tania Auchynnikava[3], Afshan McCarthy[4], Obah A. Ojarikre[5], M. Teresa Bertran[1], Anne E. Weston[6], Dan Leonce[7], Jessica Olsen[8], Kathy K. Niakan[4,9,10,11], Mark Skehel[3], James M. A. Turner[5] & Louise J. Walport[1,2,*]

Affiliations

1. Protein-Protein Interaction Laboratory, The Francis Crick Institute, London, UK
2. Department of Chemistry, Imperial College London, London, UK
3. Proteomics Science Technology Platform, The Francis Crick Institute, London, UK
4. Human Embryo and Stem Cell Laboratory, The Francis Crick Institute, London, UK
5. Sex Chromosome Biology Laboratory, The Francis Crick Institute, London, UK
6. Electron Microscopy Science Technology Platform, The Francis Crick Institute, London, UK
7. Genomics Science Technology Platform, The Francis Crick Institute, London, UK
8. Genetic Modification Service, The Francis Crick Institute, London, UK
9. The Loke Centre for Trophoblast Research, Department of Physiology, Development and Neuroscience, University of Cambridge, Cambridge, UK
10. Epigenetics Programme, Babraham Institute, Cambridge, UK
11. Wellcome–MRC Cambridge Stem Cell Institute, University of Cambridge, Cambridge, UK

* Lead contact: l.walport@imperial.ac.uk

Abstract

Oocyte cytoplasmic lattices are critical for early embryo development but their composition and function are not fully understood. Mutations in *PADI6*, an essential component of cytoplasmic lattices, lead to early embryonic developmental arrest and female infertility. To investigate PADI6 function in mRNA storage, global protein levels, and lattice composition during early mammalian development we used single cell transcriptomics and proteomics methods to study two mouse models. *Padi6* null mutation resulted in inhibition of embryonic genome activation, defective maternal mRNA degradation, and disruption to protein storage on the cytoplasmic lattices. Distinct developmental phenotypes were observed with a hypomorphic *Padi6* mutation. By developing a powerful single cell proteomic fractionation method, we define the cytoplasmic lattice enriched proteome in which we find essential components of other major oocyte-specific compartments (ELVA, MARDO), suggesting previously unknown interconnections between them. Our findings highlight a critical scaffolding function of PADI6 and implicate cytoplasmic lattices as regulatory hubs for key processes in the oocyte and early embryo, including translation, respiration and protein degradation.

Introduction

The growing oocyte stockpiles mRNA and proteins that are critical for successful fertilisation and early embryonic development[1–3]. The embryo relies on these maternally deposited factors because post-fertilization the embryonic genome is transcriptionally silent, until it is activated through a process called embryonic genome activation (EGA)[4–6]. These oocyte factors are important not only for EGA, but also for other key developmental processes such as the regulated degradation of maternal transcripts and proteins, the translation of early embryonic proteins, and the restructuring of cellular organelles such as the mitochondria and endoplasmic reticulum[1,7–10]. Loss or mutation of these maternal factors often results in developmental disorders and female infertility as a result of early embryonic developmental arrest[11–26]. How exactly they are stored and regulated remains unclear.

Various oocyte specific compartments and structures have been linked to the storage or regulation of different maternal factors and processes during oogenesis. Examples of such compartments include: the cytoplasmic lattice (CPL) for the storage of maternal proteins[7,27–30], the mitochondria-associated ribonucleoprotein domain (MARDO) for the storage of maternal mRNA[31], and the endolysosomal

58 vesicular assembly (ELVA) for degradation of protein aggregates[32]. In each case the exact
59 compositions are not fully characterised, with microscopy techniques having primarily being employed
60 to determine their composition and function[7,8,30]. Various proteins are known to be essential for CPL
61 formation, including members of the subcortical maternal complex (SCMC), comprising maternally
62 inherited proteins such as OOEP, TLE6 and NALP5, and PADI6 (peptidyl arginine deiminase 6). Early
63 studies suggested CPLs were composed of cytokeratin filaments, acting as a storage site of maternal
64 ribosomes and mRNA[7,27–29,33]. Recently however, combining bulk proteomic analyses of mouse GV
65 oocytes with super-resolution microscopy experiments and cryoelectron tomography, Schuh and co-
66 workers reported that the CPLs are instead directly composed of the SCMC and related proteins and
67 act as a storage hub not for ribosomes and mRNA, but for maternal proteins[30]. Association with the
68 CPLs is proposed to be critical for the stability of these maternal factors.
69
70 PADI6 is one of the most abundant proteins in the oocyte and early embryo and is essential for the
71 formation of the CPLs, for early embryo development and for female fertility[34–37]. 32 variants have been
72 reported as the cause of infertility in 26 women (for review see ref: [34]). Additionally female *Padi6* knock-
73 out mice are infertile, with embryonic arrest at the 2-cell stage[37]. PADI6 belongs to the peptidyl arginine
74 deiminase (PADI) family, which catalyse the post-translational conversion of peptidyl arginine to
75 citrulline in numerous protein substrates[38–42]. PADI6, however, has been reported to be inactive by *in*
76 *vitro* citrullination assays against standard PADI substrates, and its activity as an arginine deiminase
77 enzyme is yet to be confirmed[43–45]. Our recent structural characterisation of human PADI6 variants
78 highlighted that, inconsistent with a purely scaffolding function, various embryonically lethal variants do
79 not significantly damage the folded state of PADI6[45]. Given that PADI6 might have a catalytic function,
80 we aimed to de-couple scaffolding functions from catalytic functions. Using microscopy, single cell
81 transcriptomics and proteomics, we characterised oocytes and embryos from *Padi6* knock-out mice
82 and mice with an alteration in the putative catalytic site of PADI6. This revealed that catalytic activity of
83 PADI6 is not essential for female fertility and allowed us to separate developmental phenotypes
84 observed due to complete absence of the CPLs, from those due more subtle changes to the CPLs or
85 lack of an additional function of PADI6. We then developed a single cell proteomic fractionation protocol
86 to characterise the CPL-enriched proteome, which contained key factors linked not only to the CPLs,
87 but also the MARDO and ELVA, suggesting these structures may have interlinked functions. These

88 analyses provide a comprehensive list of CPL-associated proteins, defining the CPLs as regulatory
89 hubs for key cellular processes, notably protein translation, degradation, and respiration.
90

91 # Results

92 **Establishment of PADI6 catalytic mutant and knock-out mouse lines**

93 To de-couple scaffolding functions of PADI6, from potential catalytic functions, we designed a
94 catalytically inactivated PADI6 mouse model as a comparison to a complete null mutation. PADI
95 catalytic activity relies on a catalytic tetrad of residues centred on a key nucleophilic cysteine[46,47].
96 Substitution of the catalytic cysteine in PADI2 and PADI4 results in a catalytically dead enzyme. Guided
97 by multiple species sequence alignment, and our X-ray crystal structure of human PADI6, we predicted
98 that a putative catalytic function of mouse PADI6 (mPADI6) would be mediated through C663[45]. If
99 mPADI6 is catalytically active *in vivo*, substitution of C663 with alanine (mPADI6^{C663A}) would therefore
100 ablate this function by producing a catalytically dead enzyme. Any developmental phenotype observed
101 in mice expressing mPADI6^{C663A} could therefore be attributed to a loss of catalytic activity assuming
102 that protein stability was unaltered.
103

104 To confirm the cysteine to alanine substitution did not affect the stability or folded structure of mPADI6,
105 both wild-type mPADI6 and mPADI6^{C663A} were expressed and purified from mammalian cell culture
106 (**Supplementary Figures 1A-J**) and subjected to biophysical characterisation. Both the mPADI6 and
107 mPADI6^{C663A} melted at similar temperatures and formed dimers in solution with similar ratios of
108 monomer to dimer (**Supplementary Figures 1K-N**). Dimerisation is a property of PADIs 2 to 4 and
109 hPADI6 that has not previously been characterised for mPADI6[45–48]. These data indicate the C663A
110 substitution does not affect the folded dimeric structure of mPADI6.
111

112 The *Padi6*^{C663A} transgenic mouse line was then generated using CRISPR-Cas9 technology and a
113 single-stranded oligodeoxynucleotide repair template (**Supplementary Figure 2A-B**). In parallel, the
114 C57BL/6N *Padi6*$^{tm1a(KOMP)Wtsl}$/MbpMmucd line (ID:48953) was obtained from Mutant Mouse Resource &
115 Research Centers and full knock-out *Padi6*$^{-/-}$ mice were generated by crossing homozygous
116 *Padi6*^{tm1a} mice with PGK-Cre mice, resulting in the deletion of exon 4 of the *Padi6* gene
117 (**Supplementary Figure 2B**). *Padi6* transcripts were not detected in *Padi6*$^{-/-}$ ovaries, and transcript

118 levels in wild-type and *Padi6*$^{C663A/C663A}$ ovaries were not significantly different (**Supplementary Figure**
119 **2C**).
120
121 **Putative PADI6 catalytic activity is not essential for female fertility**
122 We first assessed the fertility of *Padi6*$^{C663A/C663A}$ and *Padi6*$^{-/-}$ females compared to wild-type females
123 through natural matings with wild-type C57BL/6 males over a period of 4-5 weeks. Consistent with
124 literature reports, *Padi6*$^{-/-}$ females were infertile, producing no litters (**Figure 1A**). *Padi6*$^{C663A/C663A}$
125 females on the other hand produced litters of comparable size to wild-type females (**Figure 1A**),
126 inidicating that a catalytic function of PADI6 is not essential for female fertility.
127
128 To gain a more detailed understanding of how embryos from each line were developing, we
129 characterised the developmental capacity of embryos from wild-type, *Padi6*$^{C663A/C663A}$ and *Padi6*$^{-/-}$
130 females by time-lapse imaging (**Figure 1B-C**). Unexpectedly, embryos from *Padi6*$^{C663A/C663A}$ females
131 (mat-*Padi6*$^{C663A/C663A}$) showed a small, but significant, reduction in their developmental potential
132 compared to embryos from wild-type females. Overall, 88% of wild-type zygotes successfully reached
133 the blastocyst stage compared with only 68% of mat-*Padi6*$^{C663A/C663A}$ embryos. 25% of mat-
134 *Padi6*$^{C663A/C663A}$ embryos arrested between the 4-cell and morula stages, with 7% failing at the zygote
135 and 2-cell stages, compared to wild-type embryos where only 9% arrested between the 4-cell and
136 morula stage, and 3% at zygote or 2-cell stage. Mat-*Padi6*$^{C663A/C663A}$ embryos were also delayed in
137 reaching the 2-cell, 4-cell, 8-cell and morula stages (**Figure 1D**). The most significant delay was
138 between the 4-cell and morula stages, aligning with the higher incidence of arrest observed in mat-
139 *Padi6*$^{C663A/C663A}$ embryos occurring between these stages (**Figure 1B**). Together, these observations
140 show an important but non-essential function of PADI6 was perturbed by the C663A substitution.
141
142 Embryos from *Padi6*$^{-/-}$ females (mat-*Padi6*$^{-/-}$) were considerably more restricted in their development
143 compared to both wild-type and mat-*Padi6*$^{C663A/C663A}$ embryos, with 77% arresting at the 2-cell stage, or
144 dividing to 4-cells before undergoing fragmentation and degeneration. Six embryos (14%) did progress
145 past the 4-cell stage, however all bar three exhibited fragmentation, un-synchronised and asymmetric
146 divisions, and eventual degeneration. These final three mat-*Padi6*$^{-/-}$ zygotes (7%) developed to
147 blastocysts. Mat-*Padi6*$^{-/-}$ embryos were delayed in reaching every developmental stage compared to

148 wild-type embryos, with significant delays in reaching the 2-cell to morula stages, indicative of the
149 developmental inhibition observed when PADI6 is entirely absent.
150
151 **Cytoplasmic lattices are present in *Padi6*$^{C663A/C663A}$ germinal vesicle oocytes**
152 Given the importance of PADI6 in CPL formation we used transmission electron microscopy to
153 investigate whether CPLs were perturbed in *Padi6*$^{C663A/C663A}$ germinal vesicle (GV) oocytes (**Figure 2,**
154 **Supplementary Figure 3**). In line with previous studies, there was a complete absence of CPLs in all
155 of the *Padi6*$^{-/-}$ GV oocytes tested. Contrastingly, the CPLs were present and appeared with similar
156 morphology and abundance in 5 out of 6 *Padi6*$^{C663A/C663A}$ GV oocytes, and 3 out of 4 wild-type oocytes
157 tested. This confirmed that the C663A substitution in mPADI6 does not affect the capacity of PADI6 to
158 contribute to CPL formation in mouse oocytes.
159
160 **Transcriptome dysregulation is inversely correlated in mat-*Padi6*$^{C663A/C663A}$ and mat-*Padi6*$^{-/-}$ 2-cell**
161 **embryos**
162 To investigate the role of *Padi6* on transcriptome regulation we performed scRNA-seq on MII oocytes,
163 zygotes, and dissociated blastomeres from 2-cell embryos (corresponding to the timing of EGA in mice)
164 from wild-type, *Padi6*$^{C663A/C663A}$ or *Padi6*$^{-/-}$ females (**Figure 3A**). After filtering, principal component
165 analysis (PCA) of all samples showed that cells predominantly clustered by developmental stage
166 (**Supplementary Figures 4A-D**). When compared to wild-type samples, both mat-*Padi6*$^{C663A/C663A}$ and
167 mat-*Padi6*$^{-/-}$ samples displayed significant transcriptomic dysregulation. Coinciding with EGA, this
168 dysregulation was most prominent in 2-cell embryos, where thousands of transcripts were both up and
169 down regulated (**Figure 3B**). Unexpectedly, mat-*Padi6*$^{C663A/C663A}$ and mat-*Padi6*$^{-/-}$ embryos resulted in
170 distinct transcriptome defects. There was little overlap between the up and downregulated genes in
171 samples from *Padi6*$^{C663A/C663A}$ and *Padi6*$^{-/-}$ females at each stage (**Supplementary Figure 4E**). Instead,
172 an inverse correlation was observed at the 2-cell stage; 1097 (61%) of the genes upregulated in mat-
173 *Padi6*$^{C663A/C663A}$ 2-cell embryos were downregulated in mat-*Padi6*$^{-/-}$ 2-cell embryos (**Figure 3C**). This
174 inverse effect was less prominent in the opposite direction; only 241 (31%) of the genes downregulated
175 in mat-*Padi6*$^{C663A/C663A}$ 2-cell embryos were upregulated in mat-*Padi6*$^{-/-}$ 2-cell embryos (**Figure 3C**).
176 Biological process gene ontology (GO) analysis of either the genes upregulated in mat-*Padi6*$^{C663A/C663A}$,
177 or the genes downregulated in mat-*Padi6*$^{-/-}$ 2-cell embryos, was enriched for primarily cytoplasmic

178 translation, rRNA processing, and translation, as well as mRNA processing, RNA splicing, ribosome
179 biogenesis, and ribosomal small subunit biogenesis (**Supplementary Figure 4F**). No significant
180 enrichment for any biological processes was seen in GO analysis of either the genes downregulated in
181 mat-*Padi6*$^{C663A/C663A}$ 2-cell embryos or upregulated in mat-*Padi6*$^{-/-}$ 2-cell embryos. This clear phenotypic
182 divergence observed at the 2-cell stage is likely due to unique deficiencies during EGA caused by
183 perturbation of different PADI6 functions.
184
185 **EGA is dysregulated in mat-*Padi6*$^{C663A/C663A}$ embryos and inhibited in mat-*Padi6*$^{-/-}$ embryos**
186 Differentially expressed genes were subjected to over representation analysis (ORA) by comparison
187 with a previously defined transcriptomic database of mouse early embryo development (DBTMEE v2)[49].
188 Genes involved in major EGA, and mid-pre-implantation gene activation were downregulated in mat-
189 *Padi6*$^{-/-}$ 2-cell embryos suggesting the observed developmental failure is indeed due to defective
190 activation of the embryonic genome in the absence of PADI6. Conversely, genes upregulated in mat-
191 *Padi6*$^{C663A/C663A}$ 2-cell embryos were linked with major EGA and mid-preimplantation gene activation
192 (MGA), as well as 2-cell transient, and maternal to MGA genes (**Figure 3D**). Furthermore, genes
193 belonging to the minor EGA subset were downregulated in 2-cell embryos. Together these observations
194 highlight a possible dysregulation of EGA in *Padi6*$^{C663A/C663A}$ 2-cell embryo.
195
196 To better understand this observed dysregulation, we plotted the average Z-score of all genes in our
197 data belonging to the maternal RNA, minor EGA, major EGA, 2-cell transient, maternal to MGA, and
198 MGA subsets in each of our conditions (**Figure 3E**). As expected, genes belonging to subsets
199 associated with genome activation and the 2-cell embryo (Major EGA, 2-cell transient and MGA) had
200 increasing Z-scores between the zygote and the 2-cell stage in wild-type embryos. This increase was
201 larger in mat-*Padi6*$^{C663A/C663A}$ embryos, further showing there were aberrantly increased transcript levels
202 for 2-cell stage genes relative to wild-type embryos. Conversely, there was no increase in average Z-
203 score between the zygote and the 2-cell embryo stage of mat-*Padi6*$^{-/-}$ embryos for Major EGA, 2-cell
204 transient, and MGA genes. This confirms that PADI6 is critical for successful EGA.
205
206
207

208 **Maternal RNA and minor EGA mRNA degradation is defective in mat-*Padi6*$^{-/-}$ 2-cell embryos**

209 Maternal transcripts are subject to tightly regulated and specific degradation post-fertilisation[50].
210 Surprisingly, maternal RNA appeared upregulated in mat-*Padi6*$^{-/-}$ 2-cell embryos when compared to
211 wild-type embryos (**Figure 3D**). Closer inspection showed a subset of maternal RNA decreased in z-
212 score between the zygote and 2-cell stages of wild-type and mat-*Padi6*$^{C663A/C663A}$ embryos,
213 corresponding to their degradation (**Figure 3F**). Such a decrease was not observed in mat-*Padi6*$^{-/-}$
214 embryos, suggesting that the apparent upregulation of maternal RNA genes in mat-*Padi6*$^{-/-}$ 2-cell
215 embryos is actually a result of their stabilisation or defective degradation in the absence of PADI6. A
216 similar phenomenon was observed for minor EGA genes which were degraded between the zygote and
217 2-cell stage of wild-type embryos (**Figure 3G**). Together this highlights a previously unknown
218 developmental defect associated with PADI6, the defective degradation of maternal transcripts post-
219 fertilization.

220

221 **Establishment of a single embryo proteomic workflow**

222 Our transcriptomic analyses revealed distinct defects in mat-*Padi6*$^{C663A/C663A}$ and mat-*Padi6*$^{-/-}$ embryos.
223 As oocytes store proteins as well as mRNA for future development, interrogation of both the
224 transcriptome and proteome is essential to fully understand the developmental phenotypes and
225 functions of PADI6. Bulk analyses of *Padi6* knock-out mouse GV oocytes have recently revealed that
226 loss of PADI6 leads to proteome defects that are decoupled from transcriptomic differences[30]. How this
227 proteomic dysregulation extends post-fertilisation, where we observed the most dramatic
228 developmental defects, has not yet been characterised. To address this we developed a single
229 oocyte/embryo proteomic workflow and used it to analyse GV oocytes and 2-cell embryos from wild-
230 type, *Padi6*$^{C663A/C663A}$ and *Padi6*$^{-/-}$ females (**Figure 4A**). The ability to profile single cells allowed us to
231 additionally assay individual sample heterogeneity present in wild-type, *Padi6*$^{C663A/C663A}$ and *Padi6*$^{-/-}$
232 samples. The number of proteins identified per single cell sample in our workflow was highly consistent,
233 with an average 5300 proteins per single GV oocyte, and 5800 proteins per single 2-cell embryo (**Figure**
234 **4B**), comparable in depth to the recently published One-Tip workflow[51], an alternative protocol for
235 performing single oocyte proteomics. The obtained GV oocyte proteomic data was highly consistent
236 between samples of the same genotype (**Figure 4C**). Proteomic data obtained from 2-cell embryos
237 showed greater variability, in particular for mat-*Padi6*$^{C663A/C663A}$ and mat-*Padi6*$^{-/-}$ embryos, likely

238 representative of the onset of developmental disruption as observed in the time-lapse analysis (**Figure**
239 **2**).
240
241 ***Padi6*$^{-/-}$ GV oocytes and 2-cell embryos show dramatic protein dysregulation**
242 PADI6 was the second most abundant protein overall in wild-type GV oocytes and the 14th most
243 abundant in wild-type 2-cell embryos (**Supplementary Figures 5A-B**), consistent with bulk proteomic
244 data[35]. PADI6 protein level in both GV oocytes and 2-cell embryos from *Padi6*$^{C663A/C663A}$ females was
245 not significantly different to wild-type levels, in line with our biophysical data showing the C663A
246 substitution did not affect protein expression or stability (**Supplementary Figures 5C-D**).
247
248 Globally, in *Padi6*$^{C663A/C663A}$ GV oocytes, 124 proteins were downregulated and 23 were upregulated
249 when compared to wild-type (**Figure 4D**). More pronounced dysregulation was observed in *Padi6*$^{-/-}$ GV
250 oocytes with 363 proteins downregulated and 212 proteins upregulated. At the 2-cell stage, in contrast
251 to the dramatic transcriptional dysregulation observed in mat-*Padi6*$^{C663A/C663A}$ embryos (**Figure 3B**), few
252 proteins were dysregulated, with 58 proteins downregulated, and 86 upregulated (**Figure 4D**). Again,
253 as in the GV oocyte, more pronounced dysregulation was seen in mat-*Padi6*$^{-/-}$ 2-cell embryos with 307
254 downregulated and 219 upregulated (**Figure 4D**), although this is still less substantial than the
255 transcriptomic dysregulation observed in equivalent embryos (**Figure 3B**). Overall, little to no correlation
256 was observed between mRNA and protein dysregulation in either mat-*Padi6*$^{C663A/C663A}$ or mat-*Padi6*$^{-/-}$
257 2-cell embryos (**Supplementary Figure 5E**). This is consistent with data showing that minimal
258 translation occurs in the 2-cell embryo, with the first large translational wave only occuring in the
259 morula[52], suggesting that transcriptomic and proteomic dysregulation need not be linked at early
260 developmental stages.
261
262 Similar to the distinct transcriptomic phenotypes observed, there was minimal overlap in dysregulated
263 proteins from *Padi6*$^{C663A/C663A}$ and *Padi6*$^{-/-}$ females at each stage (**Supplementary Figures 5F-G**).
264 Pathway enrichment analysis of the dysregulated proteins using the Search Tool for the Retrieval of
265 Interacting Genes/Proteins (STRING)[53] showed no significant enrichment for any biological processes
266 for those dysregulated in *Padi6*$^{C663A/C663A}$ GV oocytes. On the other hand, RNA splicing and mRNA
267 processing factors were downregulated in the *Padi6*$^{-/-}$ GV oocytes, suggesting that early genome

activation events could be misregulated due to defects in RNA processing (**Supplementary Figure 5H)**. Additionally, numerous catabolic pathways were upregulated in *Padi6*$^{-/-}$ GV oocytes, including many components in the fatty acid metabolism and β-oxidation pathway, indicating energy production pathways may be altered in the absence of PADI6 (**Supplementary Figure 5I**). As in the GV oocytes, no significant enrichment for any biological processes was observed for dysregulated proteins in mat-*Padi6*$^{C663A/C663A}$ 2-cell embryos consistent with their viability. Mat-*Padi6*$^{-/-}$ 2-cell downregulated proteins were not significantly enriched for any biological processes, however, mat-*Padi6*$^{-/-}$ 2-cell upregulated proteins enriched significantly for mRNA processing, splicing and epigenetic modification processes (**Supplementary Figure 5J**).

The levels of key CPL scaffolding proteins from the SCMC (OOEP, TLE6, NALP5 and KHDC3), were not significantly different in either *Padi6*$^{C663A/C663A}$ or *Padi6*$^{-/-}$ GV oocytes or 2-cell embryos when compared to wild-type (**Supplementary Figures 6A-B**). UHRF1 was abundantly expressed in wild-type GV oocytes and 2-cell embryos, but virtually absent in *Padi6*$^{-/-}$ GV oocytes and 2-cell embryos (**Supplementary Figure 6A-B**). This PADI6-dependent co-depletion of UHRF1 on the protein level was previously observed in bulk proteome analyses[30], and is not mirrored by a corresponding decrease in the mRNA level of UHRF1 (**Supplementary Figure 6C**), suggesting PADI6 regulates UHRF1 protein levels. No significant change in UHRF1 level was observed in GV oocytes or 2-cell embryos from *Padi6*$^{C663A/C663A}$ females compared with wild-type, ruling out a catalytic contribution to this stabilisation.

The CPLs store critical housekeeping proteins for the early embryo

Dysregulation and developmental defects in *Padi6*$^{-/-}$ GV oocytes have been linked to the absence of CPLs, which are proposed to be key regulators of protein stability in mammalian oocytes[30]. Multiple studies have highlighted the complex composition of CPLs, which appear to house multiple proteins in addition to the core members. Key structural components of the CPLs have been identified (PADI6, SCMC, UHRF1)[37,54–57], along with the recent identification of a range of proteins stored on the lattices[30]. Despite this growing understanding, however, the full composition remains uncharacterised. A complete list of the CPL components would aid in our understanding of CPL function and the phenotypes related to PADI6.

298 CPLs are Triton X-100 insoluble and historically triton extraction experiments coupled with
299 immunofluorescence have been employed to characterise CPL associated factors[7,8,33]. We reasoned
300 that Triton X-100 treatment followed by single oocyte mass spectrometry of *Padi6*$^{-/-}$ and wild-type
301 oocytes could be used to more comprehensively identify proteins associated with intact CPLs. CPL
302 associated proteins would be enriched in the Triton X-100 insoluble fraction in wild-type oocytes after
303 treatment, but washed out in *Padi6*$^{-/-}$ oocytes that lack the CPLs (**Figure 5A**). Wild-type, *Padi6*$^{C663A/C663A}$
304 and *Padi6*$^{-/-}$ GV oocytes were subjected to Triton X-100 treatment immediately after harvesting, washed
305 thoroughly in PBS and analysed using our single cell proteomics workflow. As expected for sub-cell
306 proteomics, significantly fewer proteins per oocyte were identified in Triton X-100 treated samples, with
307 an average of 1700 (**Figure 5B**). Overall sample variation for treated samples increased in comparison
308 with intact oocytes; as seen previously, more variation was also observed in *Padi6*$^{C663A/C663A}$ and *Padi6*$^{-}$
309 $^{/-}$ GV oocytes than wild-type potentially indicating heterogeneity in CPL defects (**Figure 5C**).
310
311 805 proteins were enriched in wild-type in comparison to *Padi6*$^{-/-}$ Triton X-100 treated oocytes (**Figure**
312 **5D**). Given the defect in CPL formation, we propose that most of these proteins are ones that are
313 rendered insoluble through association with the CPLs in wild-type oocytes and hence comprise a bona
314 fide CPL-associated proteome. Supportive of this interpretation among the enriched proteins were all
315 reported members of the mouse SCMC (OOEP, KHDC3L, TLE6, NALP5, NLRP2, NLRP4F, NLRP7,
316 ZBED3)[9,10,56,58–61], as well as novel CPL proteins identified by Jentoft *et al.* using expansion microscopy
317 (UHRF1, SKP1, SPIN1, YWHAZ, a-Tubulin, UBE2D2, KDM2B, NLRP14, NLRP4A, NLRP4B,
318 NLRP4F)[30] (**Figure 5E**).Together these results indicate that we have established a powerful sub-cellular
319 proteomic workflow from single mouse oocytes capable of identifying proteins associated with the
320 CPLs.
321
322 Association of proteins with the CPLs has been proposed to promote stability and storage of proteins
323 in the oocyte[30]. In line with this, the identified CPL-enriched proteins were predominantly
324 downregulated, rather than upregulated, in intact *Padi6*$^{-/-}$ GV oocytes, although the extent of
325 downregulation varied (only 38 proteins were downregulated with a $\log_2$FC < -0.5) and many proteins
326 displayed little to no change in stability (**Supplementary Figures 7A-B**). Maternal to mid-
327 preimplantation genome activation proteins were the most overrepresented subset when compared

328 with the DBTMEE v2 database, in which 94 proteins were CPL-enriched[49] (**Supplementary Figure**
329 **7C**). These proteins include a variety of factors involved in key cellular processes such as translation,
330 protein degradation, respiration and splicing. Due to their critical functions these proteins are uniformly
331 expressed from the oocyte to blastocyst stage[49]. STRING analysis of the CPL-enriched proteins
332 showed a significant enrichment for both translation, and ATP generation biological processes
333 (**Supplementary Figure 7D**). This finding suggests the CPLs are key structures in the regulation and
334 storage of crucial housekeeping proteins during early embryo development.
335
336 **Clustering of CPL-enriched proteins reveals core and accessory components**
337 Clustering of the CPL-enriched proteins by z-score across Triton X-100 treated wild-type,
338 *Padi6*$^{C663A/C663A}$, and *Padi6*$^{-/-}$ GV oocytes divided the CPL-enriched proteins into seven clusters,
339 covering three general profiles (**Figure 5F**). Proteins belonging to cluster 1 (34 proteins) were the most
340 abundant in intact wild-type oocytes, had similar levels in wild-type and *Padi6*$^{C663A/C663A}$ treated samples,
341 but were dramatically reduced in *Padi6*$^{-/-}$ GV oocytes (**Figure 5F-G, Supplementary Figure 8A**).
342 Contained within cluster 1 were PADI6, key SCMC components, an array of tubulins, as well as proteins
343 previously identified to be associated to the CPLs, including UHRF1, SKP1, SPIN1 and KDM2B
344 (**Supplementary Figure 8B**). Given the known requirement of many proteins in cluster 1 for CPL
345 formation[37,54–57], this cluster likely represents core structural components of the CPLs.
346
347 Clusters 2 and 3 (91 and 113 proteins respectively) were similar to cluster 1, in that they contained
348 proteins with similar protein abundances between wild-type and *Padi6*$^{C663A/C663A}$ Triton X-100 treated
349 oocytes, with reduced abundance in *Padi6*$^{-/-}$ oocytes, although the differences in average z-score
350 between the three mouse lines were less than for cluster 1 (**Figure 5G**). STRING analysis of cluster 2
351 enriched for protein localisation and transport processes, likely driven by the presence of six 14-3-3
352 proteins (**Supplementary Figure 8C**). Cluster 3 enriched for translation related processes
353 (**Supplementary Figure 8D**). We propose that together clusters 2 and 3 represent proteins that are not
354 themselves key for CPL formation but that are associated with the CPLs, with proteins in Cluster 2 in
355 particular acting as accessory factors involved in the storage and localisation of other proteins to the
356 CPLs.
357

358 Intriguingly, proteins belonging to clusters 4 to 7 (118, 220, 174 and 55 proteins respectively, 567 total)
359 were reduced in *Padi6*$^{C663A/C663A}$ Triton X-100 treated samples to a level similar to *Padi6*$^{-/-}$ GV oocytes,
360 with the most comparable levels for proteins in clusters 6 and 7 (**Figure 5F-G**). STRING analysis of
361 clusters 4 and 5 enriched strongly for translation related processes, like cluster 3 (**Supplementary**
362 **Figure 8E-F**). Cluster 6 enriched the most for proton motive force-driven mitochondrial ATP synthesis,
363 among other mitochondrial respiratory and electron transport chain biological processes
364 (**Supplementary Figure 8G**). Proteins belonging to cluster 7 actually had lower average z-scores in
365 *Padi6*$^{C663A/C663A}$ Triton X-100 treated samples compared to *Padi6*$^{-/-}$ (**Figure 5F-G**). STRING analysis of
366 cluster 7 did not enrich significantly for any biological processes as the other clusters did, although it
367 did contain ribosomal sub-units, mitochondrial factors, and MARDO protein LSM14B (**Supplementary**
368 **Figure 8H**). Given the CPLs are readily formed in *Padi6*$^{C663A/C663A}$ GV oocytes (**Figure 1**), these data
369 suggest that the C663A substitution, affected CPL integrity in a way that was not readily assayed by
370 transmission electron microscopy. Clusters 4 to 7 therefore represent an alternate subset of accessory
371 components which require a function of PADI6 beyond CPL formation for association with the CPLs.
372
373 **Protein translation, regulation and degradation machinery are enriched in the CPLs**
374 Early work into the CPLs reported that the CPLs act as a storage hub for maternal ribosomes and
375 mRNA, however this theory was recently disputed[7,30]. In our data, 43 large ribosomal subunit proteins
376 and 25 small ribosomal subunit proteins were enriched in wild-type compared to *Padi6*$^{-/-}$ Triton X-100
377 treated GV oocytes, suggesting the CPLs are indeed associated with maternal ribosomes (**Figure 6A**).
378 Given the number of ribosomal subunits identified, this likely represents intact ribosomes. As well as
379 ribosomal subunits, SERBP1, which promotes ribosome hibernation, and RACK1, which is known to
380 bind to ribosomes and regulate translation among other cellular processes were CPL-enriched[62–65]
381 (**Figure 6B**). This substantiates the theory that the CPLs store ribosomes, with our data additionally
382 suggesting these ribosomes are stored in a dormant state
383
384 Various proteins involved in protein degradation, including SKP1, are known to be associated with the
385 CPLs[30]. As well as SKP1, we find both CUL1 and RBX1, the other two core components of the SKP1-
386 CUL1-F-box protein (SCF) ubiquitin ligase complex, and UBE2D2, a known E2 of the complex, to be
387 CPL-enriched (**Figure 6C**). The SCF complex mediates the ubiquitination of proteins involved in the

388 cell cycle and transcription, and interacts with F-box proteins as substrate recognition adaptors [66–69]. 11
389 F-box and WD-40 domain (FBXW) proteins were also present in the CPL-enriched fraction, including
390 the well characterised SCF substrate recognition adapter FBXW11 (**Figure 6C**). These FBXW proteins
391 could resemble an array of embryo specific targeting adaptors for the regulated and timely degradation
392 of maternal factors. Along with this ubiquitination machinery, 25 proteosomal subunits were enriched
393 on the CPLs (**Supplementary Figure 9A)**. Proteosomes themselves are stored along with aggregated
394 proteins, endolysosomes and autophagosomes in the liquid-like matrix ELVAs[32]. This protein matrix is
395 formed by RUFY1 and ELVAs contain the lysosome associated LAMP1, both of which were also
396 enriched in Triton X-100 treated wild-type oocytes compared to *Padi6* knock-out (**Supplementary**
397 **Figure 9B**). Together this indicates that as well as translation machinery, the CPLs house and/or
398 regulate protein degradation machinery in the oocyte.
399
400 **The CPLs are associated with oocyte mitochondria**
401 Intriguingly, many proteins involved in ATP generation and mitochondrial respiration, in particular
402 components of the electron transport chain, were enriched in the CPLs (**Figure 6D-E**). During oocyte
403 maturation, mitochondria undergo dramatic dynein and kinesin dependent reorganisation and cluster
404 around the nucleus prior to nuclear envelope breakdown[70,71]. These mitochondria cluster into
405 membraneless compartments named mitochondria-associated ribonucleoprotein domains (MARDO),
406 whose assembly is dependent on ZAR1[31]. Unexpectedly, this MARDO component, ZAR1 and related
407 isoform ZAR1L, were enriched in the CPLs together with RNA-binding protein LSM14B which also
408 colocalises with the MARDO[31](**Figure 6D**). This association of ZAR1L and LSM14B to the CPLs was
409 disrupted in *Padi6*$^{C663A/C663A}$ GV oocytes (**Supplementary Figure 9C**).
410
411 Mitochondria in human oocytes lack Respiratory Complex I as a strategy to prevent highly damaging
412 reactive oxygen species (ROS) build up[72]. How Respiratory Complex I is stored however, is unknown.
413 52 components of Respiratory Complex I, III, IV and ATP synthase machinery were CPL-enriched
414 (**Figure 6D**). 17 of these were also less enriched in the CPL fraction of *Padi6*$^{C663A/C663A}$ oocytes
415 (**Supplementary Figure 9D**).[72] Thus Respiratory Complex I storage could be CPL-dependent, and
416 dysregulated in the absence of PADI6. Notably, three key proteins (GPX1, SOD2, and PRDX6), which
417 neutralise ROS[73], and are upregulated in times of oxidative stress, are upregulated in *Padi6*$^{-/-}$ GV

418 oocytes (**Supplementary Figure 9E**), highlighting ROS damage as a possible contributor to the severe
419 developmental phenotypes present in the absence of PADI6.
420
421 **Mitochondrial factors associate with the CPLs through PADI6**
422 Finally, with an atlas of CPL proteins in hand, we sought to identify proteins whose association to the
423 CPLs was mediated by PADI6. Due to the high numbers of mice required to perform co-
424 immunoprecipitation (co-IP) experiments directly from oocytes, we instead chose to identify PADI6
425 interactors by co-immunoprecipitation of FLAG-PADI6 expressed in transiently transfected HEK-293T
426 cells, which express many of the identified CPL associated proteins. 212 proteins were enriched when
427 immunoprecipitated with FLAG-PADI6 compared to control protein FLAG-GFP (**Supplementary**
428 **Figure 10A**). These proteins included UHRF1, UHRF2, key cell cycle proteins, mitochondrial and
429 respiratory factors, ribosomal and mitochondrial ribosome components, and 14-3-3 proteins. As with
430 the CPL-enriched proteins, STRING analysis of the PADI6 co-immunoprecipitated proteins enriched
431 strongly for translation and mitochondrial respiration related biological process (**Supplementary Figure**
432 **10B**). The co-immunoprecipitation proteomic data set showed good coverage of the CPL-enriched
433 proteins supporting our use of HEK 293T cells; out of the 805 identified CPL-enriched proteins, 665
434 (82.6%) were present in the co-immunoprecipitation dataset (**Supplementary Figure 10C**).
435
436 134 proteins enriched in the PADI6 pulldown were present in the intact GV oocyte proteome data, of
437 which 44 were CPL-enriched (**Supplementary Figures 10D-E**). These proteins include many electron
438 transport chain components including several ATP synthases (ATP5ME, ATP5MG, ATP5MK, ATP5PB,
439 and ATP5PD), three cytochrome C oxidase subunits (COX5A, COX6A1, and COX6B1), two NADH
440 dehydrogenase 1 subunits (NDUFA6 and NDUFC2) and two cytochrome B complex subunits (UQCR10
441 and UQCRB). This suggests the association between oocyte mitochondria, or the MARDOs, and the
442 CPLs could be mediated through PADI6.
443
444 In line with previous studies proposing an interaction between PADI6 and 14-3-3 proteins,[74,75] three 14-
445 3-3 proteins that we found to be CPL-enriched were enriched in the PADI6 pull-down (*Ywhab, Ywhae,*
446 *Ywhah*, **Supplementary Figure 9F, 10E**). Recently, TLE6, was also found to be critical for the stability
447 of 14-3-3 proteins and their association with the CPLs[76].As TLE6 is not expressed in HEK-293T cells,

448 the co-precipitation of PADI6 and 14-3-3 proteins suggests that association of 14-3-3 proteins to the
449 CPLs may be driven through interactions with both PADI6 and TLE6. Unlike for TLE6 though, our data
450 suggest that PADI6 does not regulate 14-3-3 protein stability as these proteins were not downregulated
451 at the protein level in intact *Padi6*$^{-/-}$ GV oocytes.
452
453 Six proteins enriched in the PADI6 pulldown were downregulated in *Padi6*$^{-/-}$ GV oocytes, but were not
454 CPL-enriched (**Supplementary Figure 10E**). Among these are proteins involved in mitotic spindle and
455 cell-cycle related RNA processing (SKA1, HAUS and RPRD1B). SKA1 is of particular note as it was
456 downregulated in *Padi6*$^{C663A/C663A}$ GV oocytes in addition to knock-out oocytes. The SKA complex is
457 critical for stabilisation of the meiotic spindle and its migration to the cortex[77–79] and in line with a possible
458 cooperative function with PADI6, it has been reported that meiotic spindle morphology is significantly
459 disrupted in *Padi6* knock-out MII oocytes[8].
460

461 # Discussion

462 PADI6 is critical for early embryo development in mice and humans, but aside from being integral to
463 CPL formation, the functions of PADI6 are unclear. In this work we have used two mouse models, a
464 knock-out and a single amino acid substituted line, to untangle CPL scaffolding dependent functions,
465 from potential catalytic functions. We further leveraged these models to develop a proteomic workflow
466 that characterised the CPL-enriched proteome, providing the most comprehensive catalogue of their
467 components to date. This validates previous hypotheses on their composition and highlights potential
468 previously unknown functions. Although we see a bias towards downregulation of proteins associated
469 with the CPLs in their absence, on the whole this effect is relatively subtle, suggesting that the main
470 function of the CPLs may be the localisation and storage of proteins e.g. to keep ribosomes and protein
471 degradation machinery inactive, rather than their stabilisation, with stabilisation of certain proteins being
472 a downstream consequence of their immobilisation.
473
474 Many oocyte specific super structures with unique functions have been reported in addition to CPLs[30]
475 including the MARDO[31] and ELVA[32]. However, with microscopy techniques primarily being employed
476 in their characterisation, the exact protein compositions and regulatory mechanisms of each are
477 unknown. Additionally, the interplay between these structures has not been studied. Key factors

478 required for the formation of these structures have been identified, notably PADI6 and the SCMC for
479 the CPLs[37,54–57], ZAR1 for MARDO[31], and RUFY1 for the ELVA[32]. Both ZAR1 and RUFY1 appeared in
480 our CPL-enriched proteome. Given the ability of these proteins to form phase-separated structures in
481 the oocyte, it is conceivable that they also contribute to CPL formation and scaffolding. Or alternatively,
482 this reveals an interdependency between the MARDO, ELVA and CPLs. Further work is required to
483 untangle the interrelations between these oocyte structures, and the commonality of proteins required
484 for their formation and regulation.
485
486 We have shown that a catalytic function of PADI6 is not essential for the formation of the CPLs, or more
487 broadly for early embryo development and female fertility. Embryos from *Padi6*$^{C663A/C663A}$ females do,
488 however, show a significantly higher incidence of arrest compared to embryos from wild-type females,
489 and 2-cell embryos showed dramatic transcriptomic dysregulation, in particular in major EGA factors.
490 The enrichment of a large subset of proteins in the CPL-fraction was reduced in *Padi6*$^{C663A/C663A}$ oocytes,
491 suggesting the structure of the CPLs in these mice was disrupted. The possibility of a non-essential
492 catalytic function of PADI6 in oogenesis and early embryo development cannot therefore be ruled out,
493 although an alternative explanation for this disruption in *Padi6*$^{C663A/C663A}$ oocytes could be that this
494 substitution in PADI6 disrupts its interaction with certain proteins, which our data suggest may include
495 ribosomal and mitochondrial electron transport chain components.
496
497 Aside from the transcriptomic and EGA dysregulation observed at the 2-cell stage, we found that a large
498 subset of mat-*Padi6*$^{C663A/C663A}$ embryos arrested or degenerated at the morula stage. This points toward
499 additional functions of PADI6 later on in development, which could be catalytic and cannot easily be
500 studied in knock-out models due to the high incidence of arrest at the 2- to 4-cell stages. It is conceivable
501 that a possible catalytic function of PADI6 in the morula could be a means to enable the dissociation of
502 the CPLs, akin to the way in which histone citrullination by PADI4 can weaken the electrostatic
503 interactions between histone tails resulting in the de-compaction of chromatin[46,80,81]. The CPLs have
504 been reported to persist until the morula stage, and the mechanism of their disassembly is unknown[52].
505 This disappearence of the CPLs is accompanied by a large wave of embryonic translation and an
506 increase in free ribosomes. Our data shows that ribosomes are associated with the CPLs, most likely
507 as a mechanism through which their activity and dormancy is regulated. It would be of interest in future

work to determine whether the CPLs persist beyond the morula stage in mat-*Padi6*$^{C663A/C663A}$ embryos and whether this is accompanied by inhibited translation.

Many variants in CPL associated genes are reported to result in severe developmental phenotypes, most commonly early embryonic developmental arrest and female infertility. For the most damaging mutations, the most common observation attributed to the developmental phenotypes is an absence of the CPLs. Our work however, highlights previously unseen nuance to the function of these proteins and what constitutes an intact CPL. For example our data on the CPL proteome highlights that association of proteins with CPLs can be disrupted even when the CPLs appear intact by microscopy. Clinical data also supports this, with a range of surface point mutations in *PADI6* having been reported to result in longer pregnancies resulting in miscarriages, and in fertile women whose offspring develop multi-locus imprinting disorders [11,17,21–25,34]. To fully understand the functions of core members of the CPLs, both in the context of the CPLs, and not, models incorporating these more subtle protein changes will be required.

Acknowledgements

This work was supported by the Francis Crick Institute which receives its core funding from Cancer Research UK (CC2030, CC2052, CC2074), the UK Medical Research Council (CC2030, CC2052, CC2074), and the Wellcome Trust (CC2030, CC2052, CC2074). Work in the laboratory of KKN was supported by the Wellcome 221856/Z/20/Z and the Wellcome Human Developmental Biology Initiative 215116/Z/18/Z. The authors thank the members of the Crick Genomics Science Technology Platform (STP), the Crick Biological Research Facility and the Crick Genetic Modification Service. In particular, the authors would like to thank Lucy Collinson of the Crick Electron Microscopy STP, Sarah Maslen of the Crick Proteomics STP and Roger George and Chloë Roustan of the Crick Structural Biology STP. Additionally, we thank Agata Zielinska of the Crick Sex Chromosome Biology Laboratory for her advice and tutelage on handling oocytes and early embryos, and Daniel Snell of the Crick Genomics STP for his advice on sequencing. The authors would also like to thank Mads Lerdrup and Eva Hoffmann of the University of Copenhagen for their insightful discussions of the work. J. P. C. W was supported by a Crick-Imperial College London studentship funded by the Department of Chemistry at Imperial College London and the Francis Crick Institute.

Author contributions

Conceptualization, L. J. W., J. M. A. T., M. T. B.;

Methodology, T. A., J. O., M. T. B., O. A. O.;

Formal Analysis, J. P. C. W., T. A.;

Investigation, J. P. C. W., T. A., A. M., A. E. W., D. L.;

Resources, O. A. O., J. M. A. T.;

Writing – Original Draft, J. P. C. W., L. J. W.;

Writing – Review & Editing, J. P. C. W., L. J. W., J. M. A. T., T. A., K. K. N.;

Visualisation, J. P. C. W.;

Supervision, L. J. W,. J. M. A. T., M. S., K. K. N.;

Project Administration, L. J. W., J. P. C. W., M. T. B.;

Funding Acquistion, L. J. W., J. M. A. T., K. K. N.;

567 # Data Availability

568 Raw and processed scRNA-seq data are available from the Gene Expression Omnibus[82], under
569 accession GSE289965. Raw and processed mass spectrometry data have been deposited to the
570 ProteomeXchange Consortium via PRIDE[83], under the identifier PDX060967. Time-lapse imaging
571 videos and transmission electron microscopy images are available from the lead contact upon request.
572 Jupyter notebooks used to analyse scRNA-seq and mass spectrometry data are available under
573 https://doi.org/10.5281/zenodo.14882496. Unprocessed western blot images are contained within the
574 Supporting Information of this publication.

575

576 # Methods

577 **Animal general husbandry**

578 All animal procedures were performed in accordance with the relevant institutional and national
579 guidelines and regulation, under the UK Home Office License Number P1234304. The animals were
580 housed at the animal facility of The Francis Crick Institute, under a 12h light/12h dark cycle, in singly
581 ventilated cages, at relative humidity between 45 and 65% and 20 – 24 °C. Reverse osmosis water and
582 autoclaved pelleted food were available 24 h to the animals. Caging, bedding, nesting material and
583 enrichments were autoclaved prior to use and changed routinely. The health of the animals was
584 monitored by daily visual checks and weekly full health checks. Adult females and males were housed
585 in separate cages in groups of 3-4 animals. Pups were genotyped for *Padi6*^{C663A} and *Padi6* knock-out
586 alleles using real time PCR with specific probes designed for each gene by Transnetyx (Cordova, TN).
587 Only homozygous females between the ages of 8 and 11 weeks bearing the desired genetic mutations
588 were used in experiments.

589

590 **Generation of Padi6 C663A mouse model**

591 Three guide RNAs (sgRNAs) were designed using CRISPOR.org[84] to cut in Exon 16 of the *Padi6* gene
592 (Supplementary Figure 2, Supplementary Table 1). A 120bp ssODN was designed to be used with all
593 three guides and containing the C663A (TGT>GCC) mutation, silent mutations for the respective
594 guides, and 58-59 bp homology arms either side (Supplementary Table 2). C57BL/6J zygotes were
595 electroporated using the Nepa21 square wave electroporator (Sonidel). 50 μL of the RNP complex

596 together with the ssODN (1.2 μM/ 6 μM/ 8 μM was placed in the chamber of a CUY505P5 electrode,
597 and the zygotes were electroporated using a poring pulse of 225 V (length: 1 ms, interval: 50 ms, #: 4,
598 D. Rate: 10%, polarity: +) and a transfer pulse of 20 V (length: 50 ms, interval: 50 ms, #: 5, D. Rate:
599 40%, polarity: +/-). Real time PCR was performed by Transnetyx (Cordova, TN) on mouse ear-snips to
600 identify eleven F0 mice preliminarily positive for the mutation. Amplicon PCR was performed on all
601 founder mice spanning the entire ssODN and submitted for high-throughput sequencing using Illumina
602 MiSeq sequencing 250 bp paired-end reads at the Crick Genomics Science Technology Platform
603 (primers listed in Supplementary Table 3). Targeting with sgRNA-3 produced six F0 mice with perfect
604 integration of the point mutations; three of these mice, with the highest percentage of the intended
605 mutation, were crossed to C57BL/6J and produced two and six F1 mice in independent lines, identified
606 as heterozygous for the mutation by Illumina MiSeq sequencing. Long read sequencing (Oxford
607 Nanopore Technologies) was performed on 3.2 kb amplicons, generated by PCR, spanning the
608 targeted insertion on a single F1 mouse from each line, no aberrant on-target mutations or deletions
609 were found 1.5 kb upstream or downstream of the insertion in either case (primers listed in
610 Supplementary Table 4). Copy number was evaluated using ddPCR on the same two F1 heterozygous
611 mice and no evidence of random integrations of the transgene was found (primers listed in
612 Supplementary Table 5).
613
614 **Generation of Padi6 knock-out mouse model**
615 C57BL/6N *Padi6*$^{tm1a(KOMP)Wtsl}$/MbpMmucd line (ID:48953) sperm was obtained from Mutant Mouse
616 Resource & Research Centres (MMRC). The critical exon was deleted by inseminating oocytes from
617 *PGK-Cre* mice by in vitro fertilization (IVF). After embryo transfer, *Padi6* mice with a lacZ tagged null
618 allele (tm1b) were generated. Mice were genotyped using real time PCR with specific probes designed
619 by Transnetyx (Cordova, TN).
620
621 **Generation of sterile XX^{Y*} mice**
622 Sterile XX^{Y*} (X-attached-Y) mice were obtained by mating C57BL/6 females to XY* mice carrying a
623 rearranged Y chromosome[85]. Recombination between an X and the Y* chromosome during male
624 meiosis results in the X^{Y*} recombinant product, in which almost the entire Y* chromosome is attached

625 to the X. Adult sterile XX^{Y*} (20 mg testis) mice are identified by testis palpation under short-term
626 inhalation anaesthesia.
627
628 **Cloning and preparation of recombinant DNA**
629 Primers were designed using SnapGene® software for In-Fusion cloning (primers listed in
630 Supplementary Table 6). The mouse *Padi6* (Twist Bioscience) and human *PADI6* (DNASU,
631 #HsCD00297377) coding sequences were amplified by PCR. The pcDNA3.1-Strep-Strep-TEV
632 (donated by Dr. Neil Q. McDonald[86]) and pcDNA3.1-3xFLAG (donated by Prof. Chris Schofield) vector
633 backbones were linearized by PCR. Amplified fragment inserts and linearised vectors were resolved by
634 gel electrophoresis in a 1% Agarose TAE gel (100 V, 30 min) in TAE buffer and extracted using the
635 PureLink™ Quick Gel Extraction Kit (Invitrogen, #K210012) following the manufacturer's protocol.
636 Fragment (~50 ng) and linearised vector (~50 ng) were combined with 2 µL 5X In-Fusion HD Enzyme
637 (Takara Bio, #639650) and mixture made up to 10 µL with Nuclease Free Water. The mixture was
638 incubated for 15 min at 50 °C and 5 µL transformed into 50 µL a *E. Coli* NEB® 5-alpha aliquot (New
639 England Biolabs, #C2987H). Plasmids were sequenced by Sanger sequencing to confirm successful
640 gene insertion and MaxiPrepped using the ZymoPURE II™ Plasmid Maxiprep kit (Zymo, #D4202)
641 before transfection into Expi293™ cells or HEK-293T cells.
642
643 **Plasmid mutagenesis**
644 Mutagenesis primers were designed to be ~35 bp in length, with a melting temperature >78 °C with a
645 GC content of ~40% terminating in C or G (primers listed in Supplementary Table 7). Mutagenesis was
646 performed by PCR following the Agilent QuickChange Protocol with PfuTurbo DNA polymerase
647 (Agilent, #600250). After PCR amplification, 1 µL Dnp1 restriction enzyme (NEB, #R0176S) was added
648 to the PCR mixture and the sample incubated at 37 °C for 1 h. After 1 h, 5 µL were transformed into a
649 E. Coli NEB® 5-alpha aliquot (New England Biolabs, #C2987H). Plasmids were sequenced by Sanger
650 sequencing to confirm presence of desired mutation and MaxiPrepped using the ZymoPURE II™
651 Plasmid Maxiprep kit (Zymo, #D4202) before transfection into Expi293™ or HEK-293T cells.
652
653 **Recombinant protein expression and purification**

654 Expi293™ cells (Gibco™, #A14527) were incubated with 150 rpm agitation, 8% CO_2, at 37 °C and
655 diluted twice weekly. For transfection, cells were counted using Vi-CELL XR counter (Beckmann
656 Coultier) and diluted to 2 x 10^6 cells/mL in pre-warmed Expi293™ Expression Medium (ThermoFisher,
657 #A1435101). 24 hours later, cells were transfected with MaxiPrepped recombinant DNA and PEI 25K™
658 (Polysciences, #23966-1) at a ratio of 1:3 (DNA: PEI) in Opti-MEM® (ThermoFisher, #11058021).
659 Cultures were then incubated for 3 days before harvesting by centrifugation at 2000 rpm for 15 min at
660 4 °C and cell pellets flash frozen in liquid nitrogen and stored at -80 °C.
661
662 Frozen transfected Expi293™ cell pellets were re-suspended in purification buffer (50 mM Tris-HCl, pH
663 7.5, 200 mM NaCl, 1 mM TCEP) with cOmplete™ EDTA-free Protease Inhibitor Cocktail tablets (Merck,
664 #73567200), 1 mg/mL Lysozyme (Sigma, #L6876-5G) and a micro-spatula of DNAse (Roche,
665 #10104159001). Cells were lysed on ice by sonication and crude lysates centrifuged at 21,000 rpm for
666 45 min before being filtered through 0.45 µm PVDF filters. Cleared cell lysate was added to
667 StrepTactin® XT 4Flow® resin (Iba, #2-5010-025) at a ratio of 2 mL packed beads per 500 mL Expi293
668 cell culture and incubated at 4 °C for 4 hours with gentle rotation. After 4 h, the unbound fraction was
669 removed by gravity filtration and the resin was washed with purification buffer. Washed resin was re-
670 suspended in twice its volume of purification buffer, TEV protease (produced in-house) added at a ratio
671 of 2 mg protease per 500 mL Expi293 cell culture and incubated at 4 °C overnight with gentle rocking.
672 The cleaved fraction was then removed by gravity filtration and the resin was again washed with
673 purification buffer. Cleaved and wash fractions were combined and concentrated to 2 mL using a
674 Vivaspin™ 20, 30000 MWCO ultrafiltration centrifugal concentrator (Sartorius, #10506282) and purified
675 by size exclusion chromatography using a HiLoadTM 16/600 SuperdexTM 200 pg Gel Filtration Column
676 (Cytivia, # 28989335), in purification buffer on an ÄKTApure™ system (Cytivia). Fractions were
677 characterised by SDS-PAGE and pooled. Pooled fractions were concentrated again until no further
678 decrease in volume was observed and stored at -80 °C.
679
680 **Intact-MS**
681 Proteins were denatured and diluted to 1 µM at pH 2 with 2% (v/v) formic acid and 2% (v/v) acetonitrile.
682 Denatured proteins were injected onto a C4 BEH 1.7 µm, 1 mm x 100 mm UPLC column (Waters™,
683 #186005590) using an Acquity I class LC (Waters™). Proteins were eluted with a 15 min gradient of

684 acetonitrile (2% v/v to 80% v/v) in 0.1% v/v formic acid using a flow rate of 50 µL/min. The analytical
685 column outlet was directly interfaced via an electrospray ionisation source, with a time-of-flight
686 BioAccord mass spectrometer (Waters™). Data was acquired over a *m/z* range of 300 – 8000, in
687 positive ion mode with a cone voltage of 40 V. Scans were summed together manually and
688 deconvoluted using MaxEnt1 (Masslynx, Waters™). Deconvoluted mass and intensity values were
689 exported and plotted in GraphPad Prism.
690
691 **Nano differential scanning fluorimetry**
692 Proteins were diluted to an approximate concentration of 0.2 mg/mL in purification buffer (50 mM Tris-
693 HCl, pH 7.5, 200 mM NaCl, 1 mM TCEP). Melting experiments were performed using Prometheus™
694 NT.48 High Sensitivity Capillaries (NanoTemper, #PR-C006-200) on a Prometheus (NanoTemper)
695 instrument with a 20 to 95 °C melt at 1 °C per minute. The 350/30 nm fluorescence ratio and first
696 derivative of this ratio was plotted against temperature using GraphPad Prism. Melting temperatures
697 were extracted as the first derivative peak in the melting curve calculated using the Panta Analysis
698 software (NanoTemper). Experiment was conducted in triplicate.
699
700 **Mass Photometry**
701 Proteins were diluted to an approximate concentration of 20 nM in purification buffer (50 mM Tris-HCl,
702 pH 7.5, 200 mM NaCl, 1 mM TCEP). 2 µL of diluted protein was then added to 18 µL of PBS in the well
703 of a gasket on a TwoMP instrument (Refeyn) and events recorded over the course of 1 min using the
704 AquireMP software (Refeyn). Molecule sizes were calculated using the AnalyseMP software (Refeyn)
705 using BSA (Thermo Scientific™, #23209), ADH (Sigma-Aldrich, #A7011) and Urease (Sigma-Aldrich,
706 #94280) as standards. Mass normalised event histograms were produced using GraphPad Prism with
707 bin sizes of 5 kDa.
708
709 **Mouse ovary RT-qPCR**
710 Ovaries were homogenised using a 21G BD Microlance™ 3 needle (Camlab, #304432) and mRNA
711 extracted using RNeasy® Mini Kit (Qiagen, #74104) following the manufacturer's protocol. Extracted
712 mRNA was reverse transcribed using the LunaScript® RT Super Mix Kit (NEB, #E3010S) following the
713 manufacturer's protocol. Transcribed mRNA was diluted in Nuclease Free Water to 5 ng/µL and RT-

714 qPCR was performed using QuantiTect® qPCR primer assays (Qiagen) for *Padi6* (Mm_Padi6_1_SG,
715 #QT00162750) and *B2m* (Mm_B2m_2_SG, #QT01149547) with the PowerUp™ SYBR™ Green
716 Master Mix (Applied Biosystems™, #A25741) following the manufacturer's protocol on a QuantStudio™
717 12K Flex Real-Time PCR System (Applied Biosystems™) instrument following the standard PowerUp™
718 SYBR™ Green PCR program.
719
720 **Evaluation of female mouse fertlity**
721 To evaluate fertility, females were mated over a period of at least 21 days with wild-type male stud mice.
722 The number of pups born per litter was recorded. 14 wild-type females produced 14 litters, 8
723 *Padi6*$^{C663A/C663A}$ females produced 8 litters, and 5 *Padi6*$^{-/-}$ females did not produce any litters.
724
725 **Timed natural matings**
726 To gather MII oocytes, females were time mated with sterile XX^{Y*} males, as previously described[85]. For
727 zygotes and 2-cell embryos, females were time mated with wild-type C57BL/6J males. Natural matings
728 were conducted as follows: females were placed into the cage of males at approximately 1700 h. The
729 following morning, the presence of a vaginal plug was taken as evidence of successful mating and
730 designated as Day 1 of gestation (E0.5).
731
732 **GV oocyte collection**
733 Female mice between the ages of 8 and 10 weeks were culled, ovaries removed and placed in 2 mL of
734 room temperature Medium2 (M2) (Sigma-Aldrich, #M7167) with 250 µM Dibutyryl cAMP (DBcAMP,
735 Sigma-Aldrich, #D0260-5MG) in a 35 mm cell culture dish (Corning, #430165). Using a Leica MC80
736 dissecting microscope, ovarian follicles were repeatedly punctured with an 30G BD Microlance™ 3
737 needle (Camlab, #304432) to release oocytes. GV oocytes were identified by presence of a clear
738 nucleus in the centre of a round cell. Oocytes were aspirated using a Stripper pipette with a 275 µm tip
739 (Cooper Surgical, #MXL3-STR and #MXL3-275), and washed five times through droplets of M2
740 medium, followed by three washes in Dulbecco's PBS (Gibco, #14190-094).
741
742
743

744 **MII oocyte collection**

745 At approximately 1700 h on the day a vaginal plug was found, females were culled, and their uteri
746 removed and placed in a 50 µL droplet of room temperature M2 medium (Sigma-Aldrich, #M7167) in a
747 60 mm dish (Corning, #430196). Using a Leica MC80 dissecting microscope, uteri were dissected using
748 surgical forceps (Dumont, #0208-5-PO) and cumulus masses were aspirated using a Stripper pipette
749 with a 275 µm tip (Cooper Surgical, #MXL3-STR and #MXL3-275). Cumulus cells were removed by
750 incubation in 3 mg/mL Hyaluronidase (Sigma-Aldrich, #H4272-30G) in FHM for 5 seconds and washed
751 five times in M2 medium, followed by three washes in Dulbecco's PBS (Gibco, #14190-094).

752

753 **Collection of zygotes**

754 At approximately 1700 h on the day a vaginal plug was found, females were culled, and oviducts were
755 removed and placed in Embryo Max® FHM medium (Sigma Aldrich, #MR-024D) in a 60 mm dish
756 (Corning, #430196). Under a Leica MC80 dissecting microscope, the infundibulum was torn using using
757 surgical forceps (Dumont, #0208-5-PO) releasing the cumulus masses. Cumulus cells were removed
758 by incubation in 3 mg/mL Hyaluronidase (Sigma-Aldrich, #H4272-30G) in FHM medium and zygotes
759 were identified by the presence of one or two polar bodies, and clearly visible pronuclei. Zygotes were
760 then washed five times in FHM medium, followed by three washes in Dulbecco's PBS (Gibco, #14190-
761 094).

762

763 **Collection of 2-cell embryos**

764 Time mated females were culled at 0900 h on Day 2 of gestation and oviducts placed Embryo Max®
765 FHM medium (Sigma Aldrich, #MR-024D) in a 60 mm dish (Corning, #430196). Using a Leica MC80
766 dissecting microscope, uteri were dissected using surgical forceps (Dumont, #0208-5-PO) and 2-cell
767 embryos were aspirated using a Stripper pipette with a 275 µm tip (Cooper Surgical, #MXL3-STR and
768 #MXL3-275). 2-cell embryos were then washed five times through droplets of FHM medium, followed
769 by three times through droplets of Dulbecco's PBS (Gibco, #14190-094).

770

771 **Dissociation of 2-cell embryos into blastomeres**

772 For scRNA-seq, 2-cell embryos were dissociated into individual blastomeres. Briefly, after an initial
773 wash in Embryo Max® FHM medium (Sigma Aldrich, #MR-024D), the zona was removed by brief

774 incubation in 1X acidic Tryode's solution (Sigma-Aldrich, #T1788) for approximately 1 min or until the
775 zona pellucida had visibly disappeared. 2-cell embryos were then washed three times in FHM medium
776 and incubated with 1X StemPro™ Accutase™ (Gibco™, #A1110501) for 5 min at room temperature.
777 Following the incubation the embryos were washed in FHM medium and dissociated into single
778 blastomeres by repeatedly aspirating and forcefully ejecting the embryo using a Stripper pipette with a
779 100 µm tip (Cooper Surgical, #MXL3-STR and #MXL3-100).
780
781 **Time-lapse imaging of zygote development to blastocyst**
782 Mouse zygotes were cultured in pre-equilibrated Global medium (LifeGlobal, #LGGG-20) supplemented
783 with 10% human serum albumin supplement (LifeGlobal, #GHSA-125) and overlaid with mineral oil
784 (Origio, #ART-4008-5P). The embryos were cultured in EmbryoSlide+ culture dishes, using an
785 EmbryoScope+ time-lapse incubator (VitroLife) at 37 ºC, 5.5% carbon dioxide (CO_2), over a period of
786 five days. Time-lapse videos of embryo development were then analysed using Fiji. Pro-nuclear fading
787 time was used to normalise the time at which the embryos reached the following stages: 2-cell, 4-cell,
788 8-cell, morula, cavity formation, and blastocyst. A total of 68 zygotes from 11 wild-type females, 84 mat-
789 zygotes from 12 *Padi6*$^{C663A/C663A}$ females, 43 zygotes from 8 *Padi6*$^{-/-}$ females were imaged.
790
791 **Transmission electron microscopy**
792 Oocytes were processed for electron microscopy using a Pelco BioWave Pro+ microwave (Ted Pella
793 Inc, Redding, USA). Samples were fixed in in 2.5% (v/v) glutaraldehyde (Taab, #G002) / 4% (v/v)
794 formaldehyde (Taab, #F017) in 0.1 M phosphate buffer (PB), pH 7.4, for one hour at RT. The steps
795 including osmium, tannic acid, sodium sulphate and ethanol dehydration and 100% acetone up to and
796 including 75% resin in acetone was performed in the Biowave, except for the phosphate buffer (PB)
797 and dH_2O wash steps, which consisted of two washes on the bench followed by two washes in the
798 Biowave without vacuum at 250 W for 40 s each. Osmium and tannic acid steps were performed in the
799 Biowave for 14 min under vacuum in 2 min cycles alternating with/without 100 W power. The
800 SteadyTemp plate was kept at 21 ºC. The sodium sulphate step was performed in the Biowave for 1min
801 under vacuum with 100 W power with the SteadyTemo plate kept at 21 ºC.
802

803 After primary fixation in 2.5% (v/v) glutaraldehyde (Taab, #G002) / 4% (v/v) formaldehyde (Taab,
804 #F017) in 0.1 M phosphate buffer (pH 7.4), samples were stained with 1% (v/v) osmium tetroxide (Taab,
805 #O012) / 1.5% (v/v) potassium ferricyanide (Sigma, #702587), washed in dH_2O, incubated in 1% (w/v)
806 tannic acid (Sigma, #702587) in 0.05 M PB, pH 7.4, washed in dH_2O followed by 1% sodium sulphate
807 in 0.05 M PB, pH 7.4 (Sigma). The samples were then washed in dH_2O and dehydrated in a graded
808 ethanol series (25%, 50%, 70%, 90%, and 100%, twice each), and in 100% acetone (3 times) at 250
809 W for 40 s without vacuum. Samples were gradually infiltrated with Epon 812 resin (Taab) with 25%
810 50% and 75% resin in acetone steps, at 250 W for 3 min each, with vacuum cycling (on/off at 30 sec
811 intervals). Samples were transferred to 100% resin overnight before mounting in embedding moulds
812 and polymerising at 60 ºC for 48 h.
813
814 To confirm the integrity of the oocytes, the resin blocks were trimmed and scans were performed at
815 either 50 kV / 4 W or 40 kV / 3 W, with no filter, 1601 projections and a pixel size of between 3.3 – 1.1
816 μm using an Xradia 510 Versa (Zeiss). The data was automatically reconstructed using Scout-and-
817 Scan™ Control System Reconstructor software (Zeiss) and viewed in TXM3DViewer software (Zeiss).
818 With the integrity of the oocytes confirmed, 350 nm sections were cut with a diamond knife on an RMC
819 Powertome Ultramicrotome (Boeckeler), stained with 1% toluidine blue in borax and viewed under a III
820 RS light microscope (Carl Zeiss UK) to locate the correct region for ultra-thin sectioning for transmission
821 electron microscopy. Seventy nm sections were collected onto 150 hexagonal copper grids, stained for
822 2 min with lead citrate and images obtained using a JEOL 1400 Flash transmission electron microscope
823 with Matataki Flash sCMOS camera. Transmission electron microscopy images were not processed or
824 adjusted, a total of 4 wild-type, 6 *Padi6*$^{C663A/C663A}$, and 4 *Padi6*$^{-/-}$ GV oocytes were imaged.
825
826 **scRNA-sequencing and analysis**
827 Three embryos from two independent females were processed for each genotype and stage, resulting
828 in a total of six MII oocytes and six zygotes per genotype. The 2-cell embryos were dissociated into
829 individual blastomeres and processed separately resulting in 12 single 2-cell blastomeres per genotype.
830 MII oocytes, zygotes and 2-cell embryo blastomeres were dispensed into 12.5 µL CDS sorting solution
831 from the Takara Smart-SeqHT kit (TakaraBio, #634439) and stored at -80 °C. Sequencing libraries
832 were prepared using the Takara Smart-SeqHT Kit (Takara Bio, #634439) according to the

833 manufacturer's instructions. Briefly, cells were lysed and polyadenylated RNA captured in a total volume
834 of 12.5 µL. One-Step first strand synthesis and double stranded cDNA amplification were carried out
835 with 18 PCR cycles. Amplified cDNA was purified via a SPRISelect (Beckman Coulter, #B23317) 1X
836 bead clean-up and eluted in 15 µL Elution Buffer. Nextera Dual Index libraries were prepared with the
837 Nextera XT kit (Illumina, #FC-131-1096). Purified cDNA was normalised to 0.2 ng/µL input and
838 tagmentation was carried out by adding 2.5 µL Tagment DNA Buffer + 1.25 µL Amplicon Tagment mix
839 to 1.25 µL cDNA. The tagmentation reaction was run for 10 min at 55 °C. A final index PCR was
840 performed after adding 2.5 µL Nextera compatible dual indices (at 10 µM) + 3.75 µL NPM PCR Mix.
841 Amplified libraries were purified via a SPRIselect (Beckman Coulter, #B23317) 0.9X bead clean-up. The
842 quality and fragment size distributions of the purified libraries was assessed by a 4200 TapeStation
843 Instrument (Agilent). Libraries were pooled and sequenced on the Illumina NovaSeq6000 in PE100
844 configuration to a read depth of at least 5M reads per sample.
845
846 Fastq files were mapped to the GRCm38 genome and converted to gene count files using Nextflow nf-
847 core/rnaseq pipeline[87] with parameters: aligner = star_rsem, genome = mm10. Transcriptomic data
848 processing was performed using the Python package ScanPy[88]. Gene count files were imported, and
849 genes were filtered to those present in at least 6 cells with 3000 minimum counts resulting in a filtered
850 dataset of 7551 genes. Counts were normalised to counts per million (CPM) and then converted to $\log_2$
851 values. PCA analysis was performed using ScanPy on the full dataset, as well as oocyte, zygote, and
852 2-cell split data. Principle components were extracted and plotted using GraphPad Prism. To identify
853 dysregulated genes, for each stage, mean $\log_2$CPM ratios (test vs. wild-type) and p-values were
854 calculated for each gene, extracted and plotted using GraphPad Prism. Those genes that had a
855 $\log_2$CPM fold change < -0.5 or > 0.5 with a p-value < 0.05 were highlighted as down and upregulated
856 respectively. GO analysis was performed using the Database for Annotation, Visualization and
857 Integrated Discovery (DAVID)[89,90], and Benjamini-Hochberg adjusted p-values extracted and plotted in
858 GraphPad Prism. Over representation analysis comparing dysregulated genes with the transcriptomic
859 database of mouse early embryo development (DBTMEE v2)[49] was performed using Python, and p-
860 values adjusted using the Benjamini-Hochberg procedure, $\log_2$(observed/expected) and -
861 $\log_{10}$(corrected p-values) were extracted and plotted using GraphPad Prism. Transcript Z-scores were
862 calculated using Python package ScanPy and plotted using the Python package matplotlib showing the

863 mean of all genes belonging to each subset with the 95% confidence interval as a shaded area above
864 and below the mean.
865
866 **Single oocyte and embryo proteomics**
867 GV oocytes and 2-cell embryos were harvested from at least 2 different females per genotype. Samples
868 were lysed in 5 µL of proteomics lysis buffer (100 mM TEAB, pH 8.5 (Sigma, # T7408-100 mL), 0.2%
869 DDM, 10 ng/µl Trypsin (Waters, #90057)) with brief sonication (10 sec in standard water bath sonicator),
870 and digested overnight at 37 °C. Following digestion samples were acidified and loaded onto Evotips
871 (Evosep, #EV2013) for MS analyses using the standard preparation procedure apart from that sample
872 loading was done by centrifugation at 400 g. Peptides were analysed using the Evosep+ 40SPD
873 Whisper method (Evosep) on an Aurora Elite column (Ion Optics). Data were acquired on a timsTOF
874 Ultra (Bruker) operated in DIA-PASEF mode with variable windows. Scan width was set between 100
875 and 1700 m/z, ion mobility window: 1/K0 0.64 – 1/KO 1.45, ramp time: 150 ms and accumulation time:
876 150 ms (data acquisition windows in Supplementary Table 8). Raw data were processed using
877 Spectronaut 18 using searching against the mouse Uniprot database (09/2022) using the default
878 settings, with local normalisation and global imputation enabled.
879
880 Locally normalised and globally imputed proteomics data was analysed using Python. Differentially
881 expressed proteins were identified as for the transcriptomic analysis. For each stage, $\log_2$ protein
882 intensity ratios (test vs. wild-type) and p-values were calculated for each protein, extracted and plotted
883 using GraphPad Prism. Those proteins that had a $\log_2$ protein intensity fold change < -0.5 or > 0.5 with
884 a p-value < 0.05 were highlighted as down and upregulated respectively. The Search Tool for the
885 Retrieval of Interacting Genes/Proteins (STRING) was used for gene ontology pathway enrichment
886 analysis of proteomics data: https://string-db.org/[53]. Enriched terms were filtered to include only those
887 with an enrichment strength > 0.5 or > 0.75, with false-discovery rate cutoffs as indicated in figure
888 legends.
889
890 **Triton X-100 treatment of GV oocytes and analysis**
891 GV oocytes from at least 2 females per genotype were characterised. GV oocytes were transferred into
892 500 µL of CPL-extraction buffer (20 mM HEPES, 100 mM KCl, 20 mM $MgCl_2$, 3 mM EGTA, 0.1% Triton

893 X-100), in a non-adherent Nunc cell culture dish (ThermoFisher, #176740) and incubated at room
894 temperature for 10 min. After 10 min, oocytes were thoroughly washed through three wells of 500 μL
895 of PBS followed by 8 x 50 μL droplets of PBS before being dispensed into 5 μL of proteomics lysis
896 buffer and stored at -80 °C. Triton X-100 treated oocytes were then processed and analysed using the
897 same single oocyte/embryo mass spectrometry workflow used for untreated samples.
898
899 Locally normalised and globally imputed proteomics data from Triton X-100 treated GV oocytes was
900 analysed using Python as for intact GV oocytes. Proteins with a $\log_2$ protein intensity ratio (*Padi6*$^{-/-}$ vs.
901 wild-type) < -0.5 and a p-value < 0.05 were classed as CPL-enriched. K-means clustering (k=7) of the
902 average z-scores of $\log_2$ transformed protein intensities of CPL-enriched proteins in Triton X-100 treated
903 wild-type, *Padi6*$^{C663A/C663A}$ and *Padi6*$^{-/-}$ GV oocytes was performed using the Python Scipy package. Z-
904 scores of $\log_2$ transformed protein intensities were ordered by cluster and plotted in GraphPad Prism.
905 Over-representation analysis was performed as for the scRNA-sequencing data. STRING analysis was
906 conducted as for proteomic data from intact GV oocytes and 2-cell embryos.
907
908 **Characterisation of human PADI6 binding proteins in HEK-293T cells**
909 Human Embryonic kidney cells (HEK 293-T, Crick Cell Services) were cultured in DMEM (Gibco™,
910 #11965092) supplemented with 10% Foetal Bovine Serum (Sigma, #F7524-50ML) with
911 Penicillin/Streptomycin (100 μg/mL, Gibco™, #15140122) in a 5% CO_2 atmosphere at 37 °C. 24 h prior
912 to transfection, cells were seeded at 1 x 10^6 cells per well of a Nunc™ cell-culture treated 6-well plate
913 (ThermoScientific™, #140675). Transient transfections were done using Lipofectamine™ 2000
914 (Invitrogen™, #11668027) in 1 mL Opti-MEM per well (ThermoScientific™, #11058021) according to
915 the manufacturer's protocol. After 4 h transfection, Opti-MEM was replaced with pre-warmed DMEM
916 (10% FBS, 100 μg/mL penicillin/streptomycin). At 48 h post-transfection, DMEM was discarded from
917 the plate and cells were washed once with cold PBS buffer. PBS was aspirated, and cells lysed with
918 immunoprecipitation buffer (50 mM Tris, pH 8.0, 50 mM KCl, 0.1% Triton X-100, 2 mM $MgCl_2$) on ice
919 for 30 min. Lysates were clarified by centrifugation at 13,000 rpm for 15 min at 4 °C, and supernatants
920 collected. 600 μL of anti-FLAG® M2 magnetic bead (Millipore, #M8823) slurry was washed in
921 immunoprecipitation buffer 3 times. Cross-linking reaction performed by adding 1 mL of 20 mM dimethyl
922 pimelimidate (Thermo Scientific™, #21666) in borate buffer, pH 9.0 (0.08 M) to the beads and rotating

923 gently at RT for 30 min. After cross-linking, beads were washed twice for 5 min in immunoprecipitation
924 buffer at RT, resuspended in 600 μL immunoprecipitation buffer and stored at 4 °C for future use. For
925 co-immunoprecipitation, 500 μL transfected cell lysate in immunoprecipitation buffer was added to 100
926 μL of conjugated anti-FLAG antibody-bead slurry in separate 1.5 mL Protein LoBind® eppendorf tubes
927 (eppendorf, #0030108116) and incubated at 4 °C for 45 min. Beads were washed 4 times with 1 mL
928 immunoprecipitation buffer (flash washes), aspirating first with a P1000 tip and second with a P200 tip
929 to ensure all supernatant was removed after each wash. 30 μL elution buffer (100 mM TEAB, 5% SDS)
930 was added to the beads, gently mixed and incubated for at 60 °C for 10 min. The eluate was collected
931 and transferred to 1.5 mL Protein LoBind® eppendorf tubes for sample processing and LC-MS/MS. Co-
932 immunoprecipitations were performed in triplicate.
933
934 Samples were digested using S-Trap™ Micro columns according to the manufacturer's protocol
935 (ProtiFi, #C02-micro-80) and digested samples loaded onto Evotips (Evosep, #EV2013). For the LC
936 separation, the standard 60SPD 2.3 method was used, separation was performed using EV-1109
937 column and the column was heated to 40 °C during analyses. Data were acquired on a timsTOF Pro2
938 (Bruker) operated in DIA PASEF mode, with scan widths set to 100-1700 m/z, IM 1K/0 0.6 - 1.6, and
939 ramp and accumulation time locked at 100 ms (data acquisition windows in Supplementary Table 9).
940
941 **Statistical analysis and reproducibility**
942 Bar charts were plotted using GraphPad Prism, with the black line representing the mean, and all data
943 points shown. Unless otherwise stated, comparison of two groups was performed using GraphPad
944 Prism using an unpaired two-tailed Student's t-test, with Welch's correction if variance was not equal
945 between groups (ns: $p > 0.05$, *: $p \leq 0.05$, **: $p \leq 0.01$, ***: $p \leq 0.001$, ****: $p \leq 0.0001$). Comparison of
946 Kaplan-Meier survival curves was performed using a log-rank Mantel-Cox test (ns: $p > 0.05$, *: $p \leq 0.05$,
947 **: $p \leq 0.01$, ***: $p \leq 0.001$, ****: $p \leq 0.0001$). For scRNA-seq and single oocyte or embryo proteomics,
948 a minimum of 6 total replicates harvested from at least 2 females were analysed for each condition.

Figures

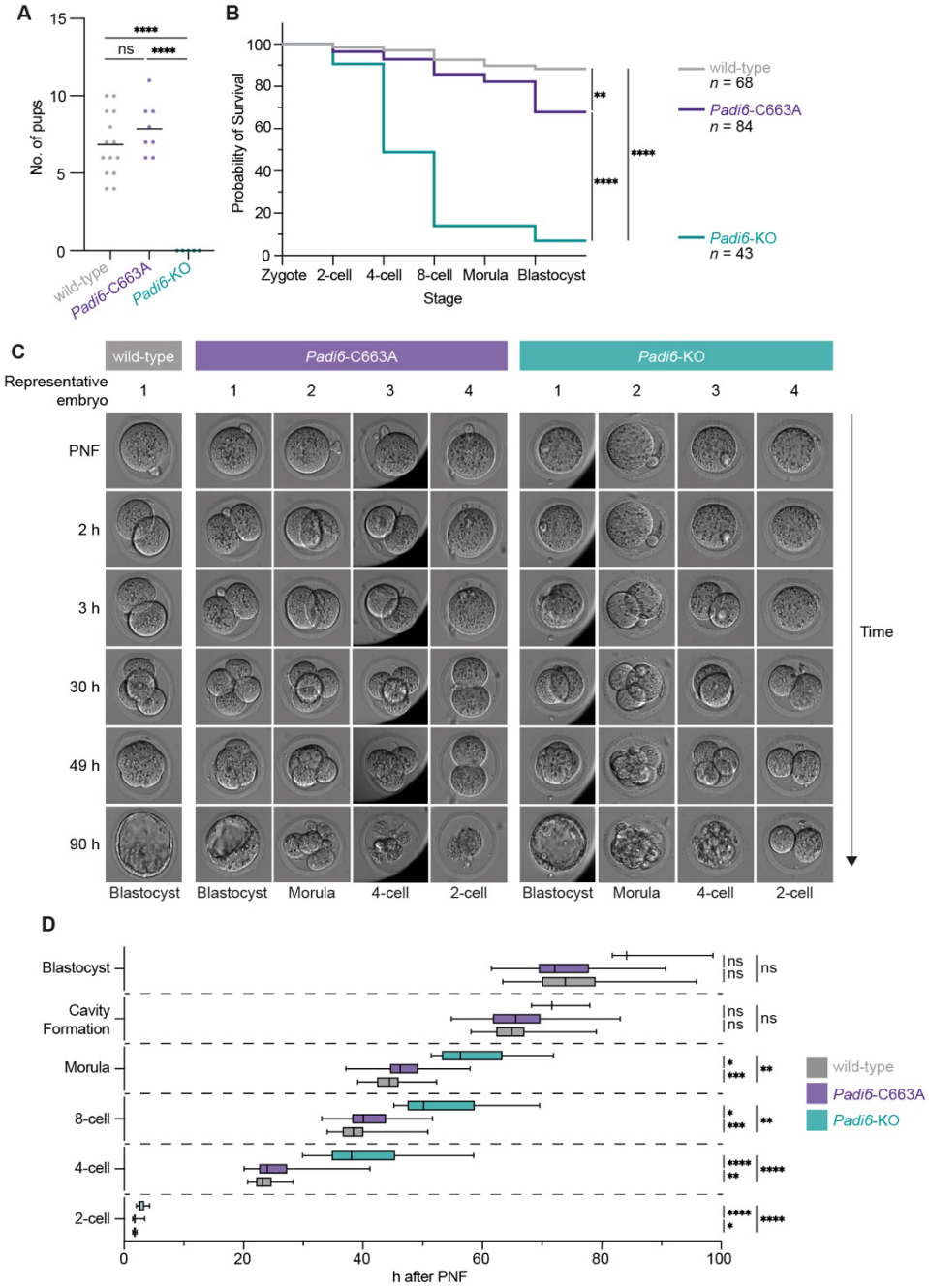

Figure 1. Mat-*Padi6*$^{C663A/C663A}$ embryos are partially inhibited in their development

(A) Litter size of wild-type (n = 14), *Padi6*$^{C663A/C663A}$ (*Padi6*-C663A, n = 8) and *Padi6*$^{-/-}$ (*Padi6*-KO, n = 5) females when naturally mated with wild-type C57BL males. Unpaired two-tailed Student's t-test; *$P \leq 0.05$, **$P \leq 0.01$, ***$P \leq 0.001$, ****$P \leq 0.0001$, ns ($P > 0.05$).
(B) Kaplan-Meier survival curve of wild-type (grey, n = 68), *Padi6*-C663A (purple, n = 84) and *Padi6*-KO (teal, n = 43) embryos. Log-rank Mantel-Cox test; *$P \leq 0.05$, **$P \leq 0.01$, ***$P \leq 0.001$, ****$P \leq 0.0001$, ns ($P > 0.05$).
(C) Representative time-lapse snapshots of embryos from wild-type, *Padi6*-C663A and *Padi6*-KO females at PNF and 2, 3, 30, 49, and 90 h post PNF. The developmental stage each embryo reached before arresting, degenerating or the end of the experiment is indicated underneath.
(D) PNF normalised times at which wild-type (grey), *Padi6*-C663A (purple) and *Padi6*-KO (teal) embryos reach key developmental stages. Unpaired two-tailed Student's t-test with Welch's correction; *$P \leq 0.05$, **$P \leq 0.01$, ***$P \leq 0.001$, ****$P \leq 0.0001$, ns ($P > 0.05$). The black central line of each box denotes the median value, the box represents the 25th to 75th percentile, and whiskers mark minimum and maximum value.

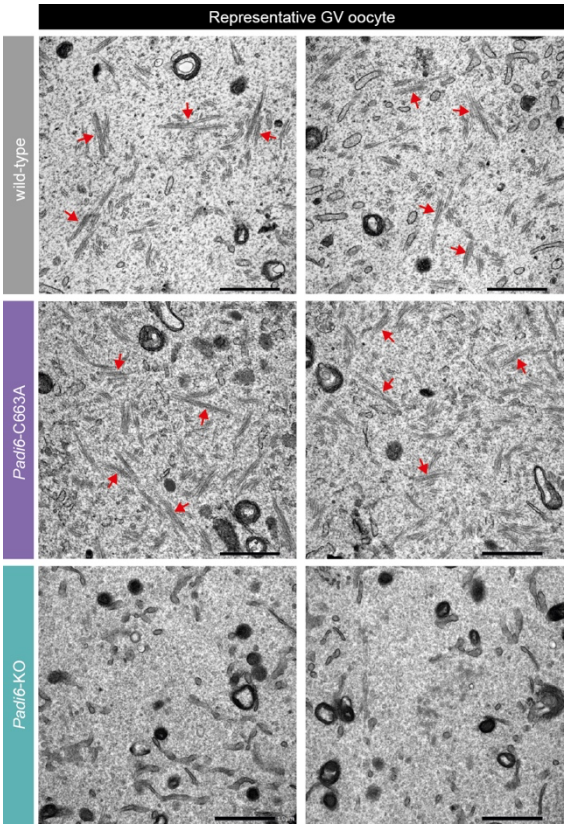

Figure 2. Cytoplasmic lattices are present in *Padi6*$^{C663A/C663A}$ germinal vesicle oocytes

Two representative transmission electron microscopy images from one wild-type, *Padi6*$^{C663A/C663A}$ (*Padi6*-C663A) and *Padi6*$^{-/-}$ (*Padi6*-KO) germinal vesicle (GV) oocyte showing CPLs are present in oocytes from wild-type and *Padi6*-C663A females, but not *Padi6*-KO females. Representative CPLs are indicated by red arrows. Scale bar = 1 µm.

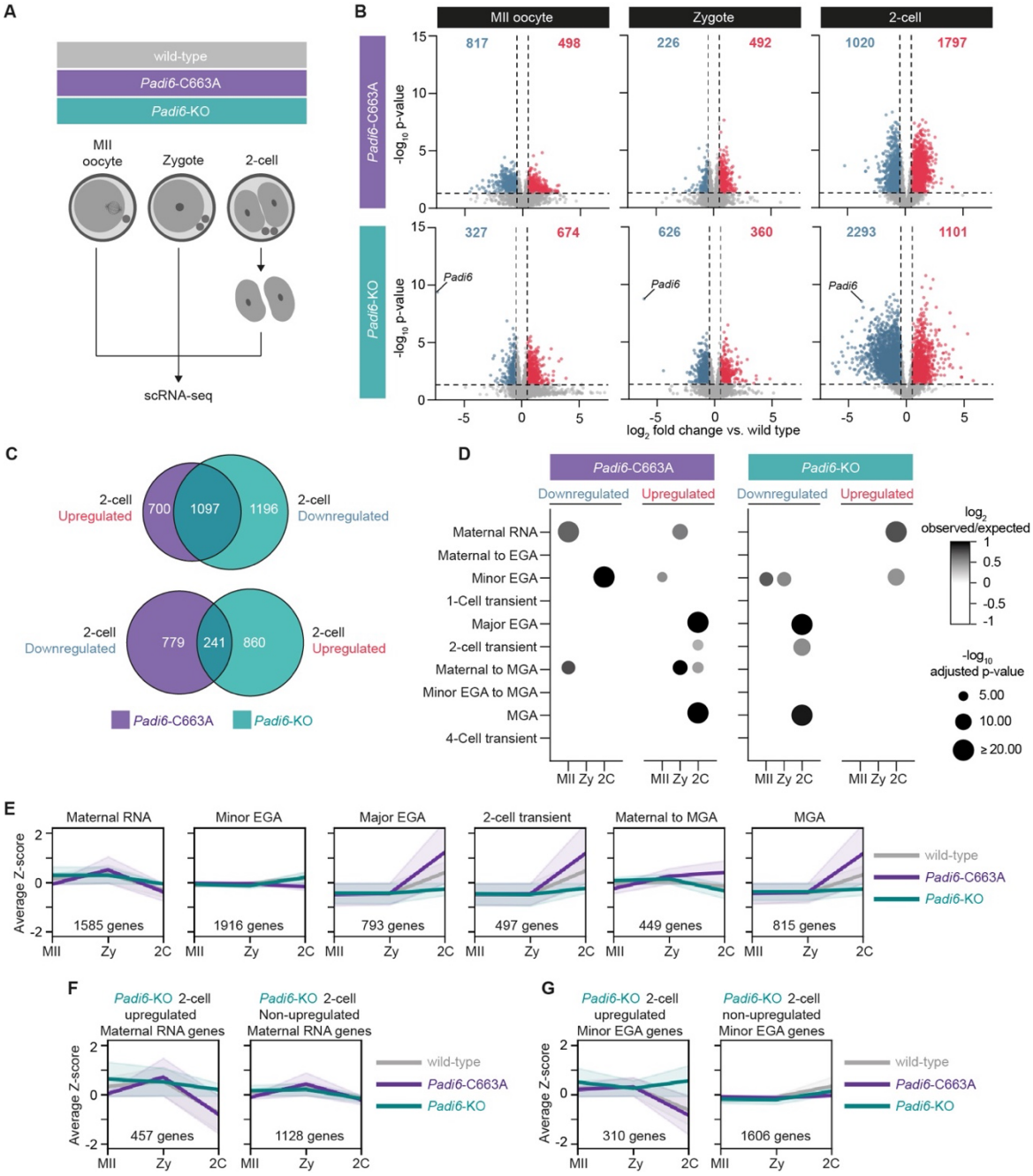

Figure 3. The transcriptome is dysregulated in mat-*Padi6*$^{C663A/C663A}$ and mat-*Padi6*$^{-/-}$ 2-cell embryos

(A) Schematic representation of the scRNA-seq experiment design. Per genetic background MII oocytes (n = 6), zygotes (n = 6), 2-cell blastomeres (n = 12).
(B) Volcano plots of differentially expressed genes in mat-*Padi6*$^{C663A/C663A}$ (*Padi6*-C663A) and mat-*Padi6*$^{-/-}$ (*Padi6*-KO) MII oocytes, zygotes and 2-cell embryos compared with wild-type. Blue points represent downregulated genes present with $\log_2$ fold change < -0.5 and p-value < 0.05. Red points represent upregulated genes present with $\log_2$ fold change > 0.5 and p-value < 0.05. Grey dashed lines indicates p-value = 0.05 and $\log_2$ fold change = -0.5 and 0.5.
(C) Venn diagram of common Padi6-C663A 2-cell upregulated and Padi6-KO 2-cell downregulated genes (upper diagram) and *Padi6*-C663A 2-cell downregulated and *Padi6*-KO 2-cell upregulated genes (lower diagram).
(D) Overlap of differentially expressed genes identified in (B) with DBTMEE v2 transcriptome categories[49]. Bubble plot sizes show $-\log_{10}$ adjusted p-values determined using a hypergeometric test for over-representation corrected for multiple testing. Bubble colour shows $\log_2$ ratio of observed gene expression changes compared with randomly expected frequencies. Under-represented genes not shown for clarity. EGA = embryonic genome activation, MGA = mid-pre-implantation gene activation.
(E) Average Z-score of all genes belonging to key DBTMEE v2 transcriptome categories[49] in MII oocytes, zygotes and 2-cell embryos from wild-type, *Padi6*-C663A and *Padi6*-KO females. Shaded area corresponds to the 95% confidence interval.
(F and G) Average Z-score of all genes belonging to the maternal RNA and Minor EGA DBTMEE v2 transcriptome categories[49] in MII oocytes, zygotes and 2-cell embryos from wild-type, *Padi6*-C663A and *Padi6*-KO females. Shaded area corresponds to 95% confidence interval. Genes are split into those that are upregulated in *Padi6*-KO 2-cell embryos and those that are not.

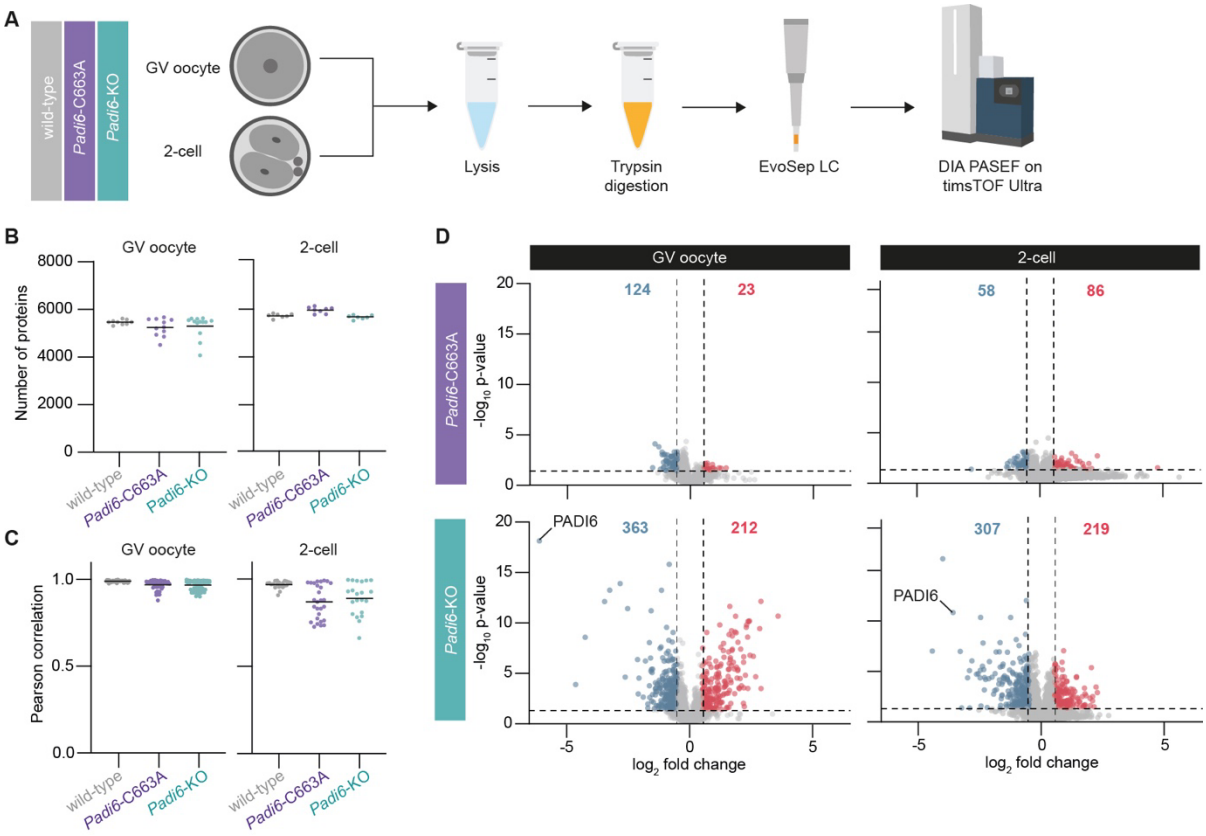

Figure 4. An absence of PADI6 results in significant protein dysregulation in GV oocytes and 2-cell embryos

(A) Schematic representation of the proteomic workflow used to characterise GV oocytes and 2-cell embryos from *Padi6*$^{C663A/C663A}$ (*Padi6*-C663A) and *Padi6*$^{-/-}$ (*Padi6*-KO) females. LC = liquid chromatography; DIA PASEF = data-independent acquisition parallel accumulation-serial fragmentation.
(B) Number of proteins identified per single oocyte/embryo for wild-type (GV oocyte n = 9, 2-cell n = 7), *Padi6*-C663A (GV oocyte n = 11, 2-cell n = 8), and *Padi6*-KO (GV oocyte n = 13, 2-cell n = 7) GV oocytes and 2-cell embryos.
(C) Pearson correlation values for wild-type, *Padi6*-C663A and *Padi6*-KO GV oocytes compared with all other GV oocytes of the same genotype.
(D) Volcano plot of differentially abundant proteins in GV oocytes and 2-cell embryos from *Padi6*-C663A and *Padi6*-KO females compared with those from wild-type females. Blue points represent downregulated proteins present with a $\log_2$ fold change < -0.5 and p-value < 0.05. Red points represent upregulated proteins present with $\log_2$ fold change > 0.5 and p-value < 0.05. Dashed lines indicates p-value = 0.05 and $\log_2$ fold change = -0.5 and 0.5.

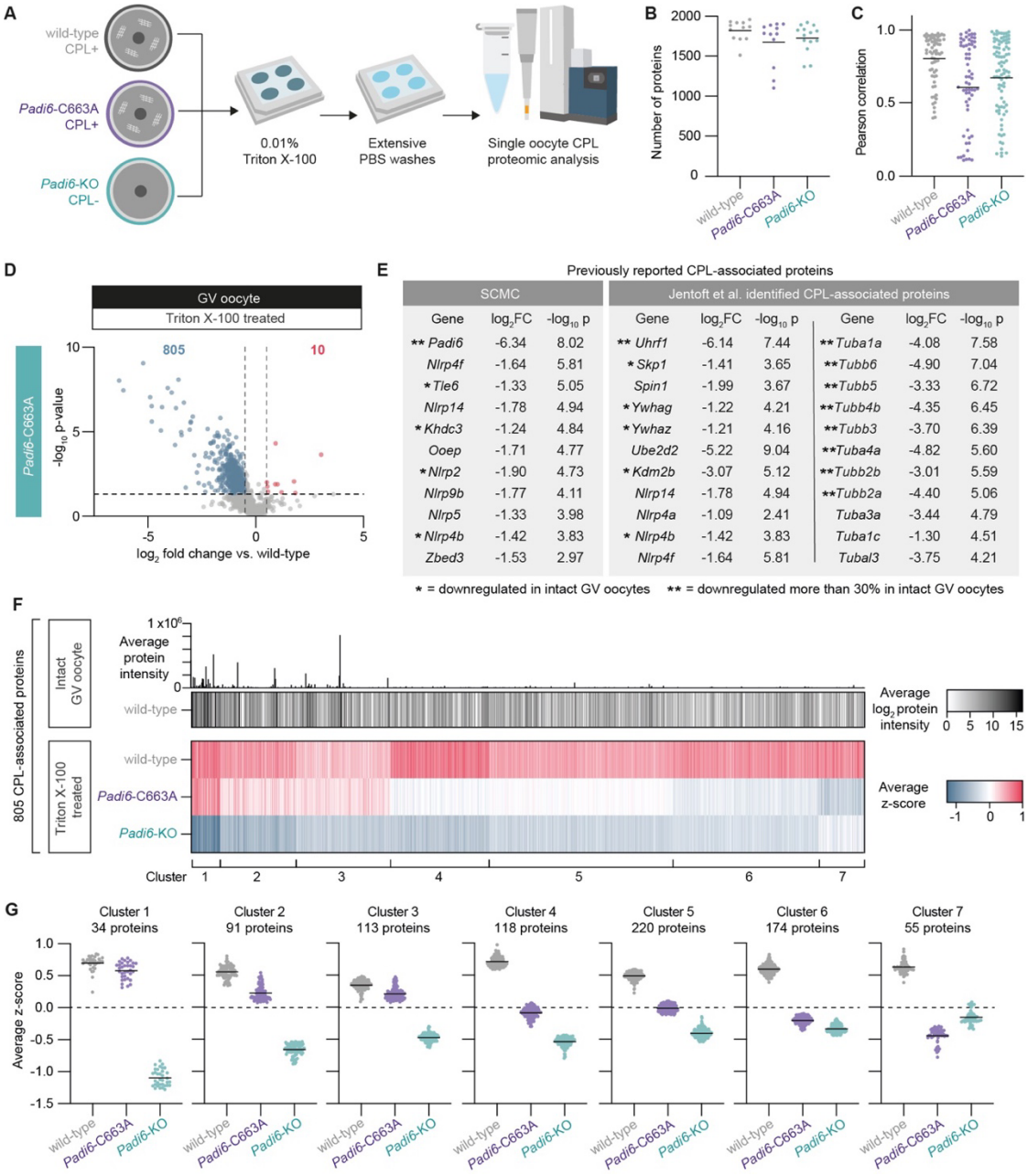

Figure 5. Characterisation of the CPL-enriched proteome

(A) Schematic representation of the experimental workflow used to identify CPL associated proteins in GV oocytes from *Padi6*$^{C663A/C663A}$ (*Padi6*-C663A) and *Padi6*$^{-/-}$ (*Padi6*-KO) females.
(B) Number of proteins identified per single oocyte for wild-type (n = 12), *Padi6*-C663A (n = 12), and *Padi6*-KO (n = 14) Triton X-100 treated GV oocytes.
(C) Pearson correlation values for wild-type, *Padi6*-C663A and *Padi6*-KO Triton X-100 treated GV oocytes compared with all other GV oocytes of the same genotype.
(D) Volcano plot of differentially abundant proteins in Triton X-100 treated GV oocytes from *Padi6*-KO females compared with Triton X-100 treated GV oocytes from wild-type females. Blue points represent downregulated proteins present with $\log_2$ fold change < -0.5 and p-value < 0.05. Red points represent upregulated proteins present with $\log_2$ fold change > 0.5 and p-value < 0.05. Dashed lines indicates p-value = 0.05 and $\log_2$ fold change = -0.5 and 0.5. Downregulated proteins are classed as CPL-enriched.
(E) Previously reported CPL proteins present in the CPL-enriched fraction of (D). Proteins grouped into SCMC components and the CPL proteins identified by Jentoft et al.[30] with $\log_2$ fold changes and $-\log_{10}$ p-values as per (D). * = downregulated between 0 and 30%, ** = downregulated >30%, intact *Padi6*-KO GV oocytes compared with wild-type.
(F) CPL-enriched proteins cluster into three main subsets. Upper panel: average protein intensities of CPL-enriched proteins in intact wild-type GV oocytes. Middle panel: heatmap of average $\log_2$ protein intensities for CPL-enriched proteins in intact wild-type GV oocytes. Lower panel: heatmap of the average z-scores of $\log_2$ transformed protein intensities of CPL-enriched proteins in Triton X-100 treated wild-type, *Padi6*-C663A and *Padi6*-KO GV oocytes, ordered by cluster after k-means clustering.
(G) Average z-scores of $\log_2$ transformed protein intensities of CPL-enriched proteins belonging to clusters 1 to 7 in Triton X-100 treated wild-type, *Padi6*-C663A and *Padi6*-KO GV oocytes.

A — CPL-associated ribosomal subunits

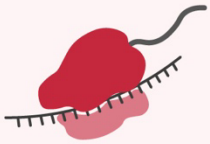

Gene	*Padi6*-KO $\log_2$FC	*Padi6*-KO $-\log_{10}$ p
Rpl10	-1.22	2.70
Rpl10a	-0.73	2.32
Rpl11	-0.78	2.17
* *Rpl12*	-0.92	2.03
* *Rpl13*	-0.75	2.23
Rpl13a	-1.08	2.96
* *Rpl14*	-0.63	2.07
* *Rpl15*	-0.84	1.65
Rpl17	-0.63	1.41
Rpl18	-0.88	2.42
Rpl18a	-1.23	4.11
Rpl19	-0.91	1.97
Rpl21	-0.80	2.24
Rpl22	-0.76	2.24
Rpl22l1	-1.39	3.69
Rpl23	-0.80	2.03
Rpl23a	-0.89	3.18
Rpl26	-1.04	2.35
Rpl27	-0.84	1.88
Rpl27a	-0.66	1.70
* *Rpl28*	-1.01	2.21
* *Rpl29*	-1.64	3.80
Rpl3	-0.76	2.10
* *Rpl30*	-1.08	2.40
Rpl31	-0.94	2.24
Rpl32	-1.02	2.55
Rpl34	-1.02	2.92
Rpl35	-1.03	2.91
Rpl35a	-0.69	1.78
Rpl36	-0.97	2.24
Rpl36a	-1.02	3.15
Rpl37a	-0.84	1.44
Rpl38	-1.79	3.14
Rpl39	-0.83	1.34
Rpl4	-0.71	1.88
* *Rpl5*	-0.68	1.36
Rpl6	-0.84	2.81
Rpl7	-1.05	2.76
* *Rpl7a*	-1.11	3.28
Rpl8	-1.21	3.24
* *Rplp0*	-0.74	1.96
Rplp2	-0.80	1.84
Uba52	-0.89	2.01

Large ribosomal subunit (43 total)

Gene	*Padi6*-KO $\log_2$FC	*Padi6*-KO $-\log_{10}$ p
** *Fau*	-0.76	2.21
Rps11	-0.82	2.52
Rps12	-0.52	2.02
Rps13	-1.05	2.70
* *Rps14*	-0.85	2.33
Rps15a	-0.67	1.83
Rps16	-0.86	2.67
Rps18	-0.80	2.00
* *Rps19*	-1.15	3.63
Rps2	-0.78	2.32
Rps21	-0.75	2.44
* *Rps23*	-0.89	2.27
Rps25	-1.19	3.09
Rps27	-0.96	2.29
Rps27l	-0.86	1.77
** *Rps29*	-0.73	1.75
Rps3	-0.73	2.26
Rps3a	-0.75	1.85
Rps4x	-0.80	2.10
* *Rps5*	-1.36	2.92
Rps6	-0.89	2.54
Rps7	-0.78	2.37
Rps8	-0.78	2.36
Rps9	-0.98	3.29
* *Rpsa*	-0.72	2.22

Small ribosomal subunit (25 total)

B — Ribosome regulatory factors

Gene	*Padi6*-KO $\log_2$FC	*Padi6*-KO $-\log_{10}$ p	
* *Serbp1*	-0.70	1.69	← Ribosome hibernation
* *Rack1*	-0.69	1.76	← Translation regulation

C — SCF complex components

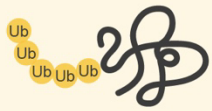

Gene	*Padi6*-KO $\log_2$FC	*Padi6*-KO $-\log_{10}$ p	
Cul1	-2.08	4.31	Core SCF complex
* *Skp1*	-1.41	3.65	Core SCF complex
* *Rbx1*	-1.28	2.63	Core SCF complex
Ube2d2	-5.22	9.04	← SCF E2 enzyme
Fbxw11	-0.89	2.77	Substrate recognition
** *Fbxw13*	-2.93	5.89	Substrate recognition
* *Fbxw14*	-1.22	4.12	Substrate recognition
** *Fbxw16*	-3.91	7.31	Substrate recognition
* *Fbxw18*	-1.72	4.68	Substrate recognition
** *Fbxw19*	-4.83	6.51	Substrate recognition
** *Fbxw20*	-3.46	4.97	Substrate recognition
** *Fbxw21*	-3.59	8.07	Substrate recognition
Fbxw22	-0.92	1.79	Substrate recognition
** *Fbxw26*	-3.02	5.53	Substrate recognition
* *Fbxw27*	-0.96	2.34	Substrate recognition

D — MARDO factors

Gene	*Padi6*-KO $\log_2$FC	*Padi6*-KO $-\log_{10}$ p
Zar1	-0.93	1.82
* *Zar1l*	-0.93	2.04
Lsm14b	-0.80	1.59

* = downregulated in intact GV oocytes

** = downregulated more than 30% in intact GV oocytes

E — Mitochondrial electron transport chain factors

Gene	*Padi6*-KO $\log_2$FC	*Padi6*-KO $-\log_{10}$ p
Ndufa12	-0.67	1.36
Ndufa2	-0.86	2.56
Ndufa4	-0.74	2.10
Ndufa5	-0.80	1.45
Ndufa6	-0.54	1.58
Ndufb3	-0.56	1.31
Ndufb5	-0.99	2.46
Ndufb6	-0.70	1.70
Ndufc2	-0.99	3.27
Ndufs1	-0.60	1.41
Ndufs2	-0.54	1.43
Ndufs4	-0.71	1.96
Ndufs5	-0.80	2.05
Ndufs7	-0.61	1.37
Ndufv1	-0.69	1.98
Ndufv3	-0.73	1.38
Cyc1	-1.16	3.42
Mt-Cyb	-0.79	1.67
Uqcrfs1	-0.70	2.13
Uqcrc1	-1.13	3.09
Uqcrc2	-0.85	2.64
Uqcr10	-1.04	2.84
Uqcrb	-1.00	2.77
Uqcrh	-1.03	1.61
Uqcrq	-1.33	3.35
* *Cox4i1*	-1.12	2.33
* *Cox5a*	-0.71	2.39
Cox5b	-0.82	1.72
Cox6a1	-0.90	2.54
Cox6b1	-1.34	2.48
Cox6c	-1.14	3.53
Cox7a2l	-1.28	1.84
Atp11c	-0.92	2.28
Atp13a1	-1.10	2.78
Atp1a1	-0.82	1.47
Atp2a2	-0.97	3.17
Atp2c1	-0.71	1.38
Atp5f1a	-0.51	1.46
Atp5f1b	-0.52	1.33
Atp5f1c	-0.75	1.91
* *Atp5if1*	-2.34	3.52
Atp5me	-1.27	2.78
Atp5mg	-0.95	2.62
Atp5mj	-1.38	1.55
Atp5mk	-2.23	2.81
Atp5pb	-0.68	1.77
Atp5pd	-0.90	1.98
Atp5pf	-0.74	1.82
Atp5po	-1.04	2.19
Atp6v0a2	-0.72	1.67
Atp8a1	-0.58	2.09
Mtatp6	-1.07	1.72

Figure 6. The CPLs are associated with protein translation, regulation and degradation machinery, and the oocyte mitochondria

(A) All large (43 total) and small (25 total) ribosomal sub-units found to be CPL-enriched with the $\log_2$ fold-change and $-\log_{10}$ p-values of Triton X-100 treated *Padi6*$^{-/-}$ (*Padi6*-KO) GV oocytes compared with Triton X-100 treated wild-type GV oocytes.
(B) Ribosome regulatory factors found to be CPL-enriched with $\log_2$ fold changes and $-\log_{10}$ p-values as per (A).
(C) Proteins associated with the SCF complex found to be CPL-enriched with $\log_2$ fold changes and $-\log_{10}$ p-values as per (A).
(D) Key MARDO factors found to be CPL-enriched with $\log_2$ fold changes and $-\log_{10}$ p-values as per (A).
(E) Mitochondrial electron transport chain factors found to be CPL-enriched with $\log_2$ fold changes and $-\log_{10}$ p-values as per (A).
* = proteins downregulated in intact *Padi6*-KO GV oocytes. ** = proteins downregulated more than 30% in intact *Padi6*-KO GV oocytes.

1042 ## References

1043 1. Li, L., Zheng, P. & Dean, J. Maternal control of early mouse development. *Development* **137**,
1044 859–870 (2010).
1045 2. Zhang, K. & Smith, G. W. Maternal control of early embryogenesis in mammals. *Reprod. Fertil.*
1046 *Dev.* **27**, 880 (2015).
1047 3. Wu, D. & Dean, J. Maternal factors regulating preimplantation development in mice. *Curr. Top.*
1048 *Dev. Biol.* **140**, 317–340 (2020).
1049 4. Tadros, W. & Lipshitz, H. D. The maternal-to-zygotic transition: a play in two acts. *Development*
1050 **136**, 3033–3042 (2009).
1051 5. Jukam, D., Shariati, S. A. M. & Skotheim, J. M. Zygotic Genome Activation in Vertebrates. *Dev.*
1052 *Cell* **42**, 316–332 (2017).
1053 6. Schulz, K. N. & Harrison, M. M. Mechanisms regulating zygotic genome activation. *Nat. Rev.*
1054 *Genet.* **20**, 221–234 (2019).
1055 7. Yurttas, P. *et al.* Role for PADI6 and the cytoplasmic lattices in ribosomal storage in oocytes and
1056 translational control in the early mouse embryo. *Development* **135**, 2627–2636 (2008).
1057 8. Kan, R. *et al.* Regulation of mouse oocyte microtubule and organelle dynamics by PADI6 and the
1058 cytoplasmic lattices. *Dev. Biol.* **350**, 311–322 (2011).
1059 9. Yu, X. J. *et al.* The subcortical maternal complex controls symmetric division of mouse zygotes by
1060 regulating F-actin dynamics. *Nat. Commun.* **5**, 4887 (2014).
1061 10. Gao, Z. *et al.* Zbed3 participates in the subcortical maternal complex and regulates the
1062 distribution of organelles. *J. Mol. Cell Biol.* **10**, 74–88 (2018).
1063 11. Rezaei, M. *et al.* Novel pathogenic variants in NLRP7, NLRP5, and PADI6 in patients with
1064 recurrent hydatidiform moles and reproductive failure. *Clin. Genet.* **99**, 823–828 (2021).
1065 12. Dong, J. *et al.* Novel biallelic mutations in PADI6 in patients with early embryonic arrest. *J. Hum.*
1066 *Genet.* 1–9 (2022) doi:10.1038/s10038-021-00998-8.
1067 13. Xu, Y. *et al.* Novel Homozygous PADI6 Variants in Infertile Females with Early Embryonic Arrest.
1068 *Front. Cell Dev. Biol.* **10**, 1–8 (2022).
1069 14. Xu, Y. *et al.* Mutations in PADI6 Cause Female Infertility Characterized by Early Embryonic
1070 Arrest. *Am. J. Hum. Genet.* **99**, 744–752 (2016).

1071 15. Zheng, W. *et al.* New biallelic mutations in PADI6 cause recurrent preimplantation embryonic
1072 arrest characterized by direct cleavage. *J. Assist. Reprod. Genet.* **37**, 205–212 (2020).
1073 16. Liu, J. *et al.* Two novel mutations in PADI6 and TLE6 genes cause female infertility due to arrest
1074 in embryonic development. *J. Assist. Reprod. Genet.* **38**, 1551–1559 (2021).
1075 17. Wang, X. *et al.* Novel mutations in genes encoding subcortical maternal complex proteins may
1076 cause human embryonic developmental arrest. *Reprod. Biomed. Online* **36**, 698–704 (2018).
1077 18. Maddirevula, S. *et al.* The human knockout phenotype of PADI6 is female sterility caused by
1078 cleavage failure of their fertilized eggs. *Clin. Genet.* **91**, 344–345 (2017).
1079 19. Zhang, T., Liu, P., Yao, G., Zhang, X. & Cao, C. A complex heterozygous mutation in PADI6
1080 causes early embryo arrest: A case report. *Front. Genet.* **13**, 1104085 (2023).
1081 20. Qian, J. *et al.* Biallelic PADI6 variants linking infertility, miscarriages, and hydatidiform moles. *Eur.*
1082 *J. Hum. Genet.* **26**, 1007–1013 (2018).
1083 21. Eggermann, T. *et al.* Trans-acting genetic variants causing multilocus imprinting disturbance
1084 (MLID): common mechanisms and consequences. *Clin. Epigenetics* **14**, 1–17 (2022).
1085 22. Eggermann, T., Kadgien, G., Begemann, M. & Elbracht, M. Biallelic PADI6 variants cause
1086 multilocus imprinting disturbances and miscarriages in the same family. *Eur. J. Hum. Genet.* **29**,
1087 575–580 (2021).
1088 23. Begemann, M. *et al.* Maternal variants in NLRP and other maternal effect proteins are associated
1089 with multilocus imprinting disturbance in offspring. *J. Med. Genet.* **55**, 497–504 (2018).
1090 24. Cubellis, M. V. *et al.* Loss-of-function maternal-effect mutations of PADI6 are associated with
1091 familial and sporadic Beckwith-Wiedemann syndrome with multi-locus imprinting disturbance.
1092 *Clin. Epigenetics* **12**, 139 (2020).
1093 25. Tannorella, P. *et al.* Germline variants in genes of the subcortical maternal complex and
1094 Multilocus Imprinting Disturbance are associated with miscarriage / infertility or Beckwith –
1095 Wiedemann progeny. *Clin. Epigenetics* **14**, 1–7 (2022).
1096 26. Demond, H. *et al.* A KHDC3L mutation resulting in recurrent hydatidiform mole causes genome-
1097 wide DNA methylation loss in oocytes and persistent imprinting defects post-fertilisation. *Genome*
1098 *Med.* **11**, 1–14 (2019).

1099 27. Capco, D. G., Gallicano, G. I., McGaughey, R. W., Downing, K. H. & Larabell, C. A. Cytoskeletal
1100 sheets of mammalian eggs and embryos: A lattice-like network of intermediate filaments. *Cell*
1101 *Motil. Cytoskeleton* **24**, 85–99 (1993).
1102 28. McGaughey, R. W. & Capco, D. G. Specialized cytoskeletal elements in mammalian eggs:
1103 Structural and biochemical evidence for their composition. *Cell Motil. Cytoskeleton* **13**, 104–111
1104 (1989).
1105 29. Ian Gallicano, G., Larabell, C. A., McGaughey, R. W. & Capco, D. G. Novel cytoskeletal elements
1106 in mammalian eggs are composed of a unique arrangement of intermediate filaments. *Mech.*
1107 *Dev.* **45**, 211–226 (1994).
1108 30. Jentoft, I. M. A. *et al.* Mammalian oocytes store proteins for the early embryo on cytoplasmic
1109 lattices. *Cell* **186**, 5308-5327.e25 (2023).
1110 31. Cheng, S. *et al.* Mammalian oocytes store mRNAs in a mitochondria-associated membraneless
1111 compartment. **262**, (2022).
1112 32. Zaffagnini, G. *et al.* Mouse oocytes sequester aggregated proteins in degradative super-
1113 organelles. *Cell* **187**, 1109-1126.e21 (2024).
1114 33. Liu, X. *et al.* Role for PADI6 in securing the mRNA-MSY2 complex to the oocyte cytoplasmic
1115 lattices. *Cell Cycle* **16**, 360–366 (2017).
1116 34. Williams, J. P. C. & Walport, L. J. PADI6: What we know about the elusive fifth member of the
1117 peptidyl arginine deiminase family. *Philos. Trans. R. Soc. B Biol. Sci.* **378**, 20220242 (2023).
1118 35. Gao, Y. *et al.* Protein Expression Landscape of Mouse Embryos during Pre-implantation
1119 Development. *Cell Rep.* **21**, 3957–3969 (2017).
1120 36. Wright, P. W. *et al.* ePAD, an oocyte and early embryo-abundant peptidylarginine deiminase-like
1121 protein that localizes to egg cytoplasmic sheets. *Dev. Biol.* **256**, 74–89 (2003).
1122 37. Esposito, G. *et al.* Peptidylarginine deiminase (PAD) 6 is essential for oocyte cytoskeletal sheet
1123 formation and female fertility. *Mol. Cell. Endocrinol.* **273**, 25–31 (2007).
1124 38. Horibata, S., Coonrod, S. A. & Cherrington, B. D. Role of PADs in Disease and Female
1125 Reproduction. *J. Reprod. Dev.* **58**, (2012).
1126 39. Witalisom, E., Thompson, R. & Hofseth, L. Protein Arginine Deiminases and Associated
1127 Cirtullination. *Curr Drug Targets* **16**, 700–710 (2015).

1128 40. Lewallen, D. M. *et al.* Chemical Proteomic Platform to Identify Citrullinated Proteins. *ACS Chem.*
1129 *Biol.* **10**, 2520–2528 (2015).
1130 41. Mondal, S. & Thompson, P. R. Protein Arginine Deiminases (PADs): Biochemistry and Chemical
1131 Biology of Protein Citrullination. *Acc. Chem. Res.* **52**, 818–832 (2019).
1132 42. Rebak, A. S. *et al.* A quantitative and site-specific atlas of the citrullinome reveals widespread
1133 existence of citrullination and insights into PADI4 substrates. *Nat. Struct. Mol. Biol.* **31**, 977–995
1134 (2024).
1135 43. Taki, H. *et al.* Purification of enzymatically inactive peptidylarginine deiminase type 6 from mouse
1136 ovary that reveals hexameric structure different from other dimeric isoforms. *Adv. Biosci.*
1137 *Biotechnol.* **02**, 304–310 (2011).
1138 44. Ranaivoson, F. M. *et al.* Crystal structure of human peptidylarginine deiminase type VI (PAD6)
1139 provides insights into its inactivity. *IUCrJ* **11**, 395–404 (2024).
1140 45. Williams, J. P. C. *et al.* Structural insight into the function of human peptidyl arginine deiminase 6.
1141 *Comput. Struct. Biotechnol. J.* **23**, 3258–3269 (2024).
1142 46. Arita, K. *et al.* Structural basis for Ca2+-induced activation of human PAD4. *Nat. Struct. Mol. Biol.*
1143 **11**, 777–783 (2004).
1144 47. Slade, D. J. *et al.* Protein arginine deiminase 2 binds calcium in an ordered fashion: Implications
1145 for inhibitor design. *ACS Chem. Biol.* **10**, 1043–1053 (2015).
1146 48. Rechiche, O., Lee, T. V. & Lott, J. S. Structural characterization of human peptidyl-arginine
1147 deiminase type III by X-ray crystallography. *Acta Crystallogr. Sect. F Struct. Biol. Commun.* **77**,
1148 334–340 (2021).
1149 49. Park, S.-J., Shirahige, K., Ohsugi, M. & Nakai, K. DBTMEE: a database of transcriptome in
1150 mouse early embryos. *Nucleic Acids Res.* **43**, D771–D776 (2015).
1151 50. Yang, G., Xin, Q. & Dean, J. Degradation and translation of maternal mRNA for embryogenesis.
1152 *Trends Genet.* **40**, 238–249 (2024).
1153 51. Ye, Z. *et al.* One-Tip enables comprehensive proteome coverage in minimal cells and single
1154 zygotes. *Nat. Commun.* **15**, 2474 (2024).
1155 52. Israel, S. *et al.* An integrated genome-wide multi-omics analysis of gene expression dynamics in
1156 the preimplantation mouse embryo. *Sci. Rep.* **9**, 13356 (2019).

1157 53. Szklarczyk, D. *et al.* The STRING database in 2021: customizable protein–protein networks, and
1158 functional characterization of user-uploaded gene/measurement sets. *Nucleic Acids Res.* **49**,
1159 D605–D612 (2021).
1160 54. Tashiro, F. *et al.* Maternal-effect gene Ces5/Ooep/Moep19/Floped is essential for oocyte
1161 cytoplasmic lattice formation and embryonic development at the maternal-zygotic stage transition.
1162 *Genes Cells* **15**, 813–828 (2010).
1163 55. Kim, B., Kan, R., Anguish, L., Nelson, L. M. & Coonrod, S. A. Potential role for MATER in
1164 cytoplasmic lattice formation in murine oocytes. *PLoS ONE* **5**, 1–8 (2010).
1165 56. Qin, D. *et al.* The subcortical maternal complex protein Nlrp4f is involved in cytoplasmic lattice
1166 formation and organelle distribution. *Development* **146**, dev.183616 (2019).
1167 57. Uemura, S. *et al.* UHRF1 is essential for proper cytoplasmic architecture and function of mouse
1168 oocytes and derived embryos. *Life Sci. Alliance* **6**, e202301904 (2023).
1169 58. Li, L., Baibakov, B. & Dean, J. A Subcortical Maternal Complex Essential for Preimplantation
1170 Mouse Embryogenesis. *Dev. Cell* **15**, 416–425 (2008).
1171 59. Mahadevan, S. *et al.* Maternally expressed NLRP2 links the subcortical maternal complex
1172 (SCMC) to fertility, embryogenesis and epigenetic reprogramming. *Sci. Rep.* **7**, (2017).
1173 60. Monk, D., Sanchez-Delgado, M. & Fisher, R. NLRPS, the subcortical maternal complex and
1174 genomic imprinting. *Reproduction* **154**, R161–R170 (2017).
1175 61. Han, J. *et al.* NLRP7 participates in the human subcortical maternal complex and its variants
1176 cause female infertility characterized by early embryo arrest. *J. Mol. Med.* **101**, 717–729 (2023).
1177 62. Anger, A. M. *et al.* Structures of the human and Drosophila 80S ribosome. *Nature* **497**, 80–85
1178 (2013).
1179 63. Sundaramoorthy, E. *et al.* ZNF598 and RACK1 Regulate Mammalian Ribosome-Associated
1180 Quality Control Function by Mediating Regulatory 40S Ribosomal Ubiquitylation. *Mol. Cell* **65**,
1181 751-760.e4 (2017).
1182 64. Smith, P. R. *et al.* Functionally distinct roles for eEF2K in the control of ribosome availability and
1183 p-body abundance. *Nat. Commun.* **12**, 6789 (2021).
1184 65. Shetty, S., Hofstetter, J., Battaglioni, S., Ritz, D. & Hall, M. N. TORC1 phosphorylates and inhibits
1185 the ribosome preservation factor Stm1 to activate dormant ribosomes. *EMBO J.* **42**, e112344
1186 (2023).

1187 66. Li, Y. & Hao, B. Structural Basis of Dimerization-dependent Ubiquitination by the SCFFbx4
1188 Ubiquitin Ligase. *J. Biol. Chem.* **285**, 13896–13906 (2010).
1189 67. Zheng, N. *et al.* Structure of the Cul1–Rbx1–Skp1–F boxSkp2 SCF ubiquitin ligase complex.
1190 *Nature* **416**, 703–709 (2002).
1191 68. Cardozo, T. & Pagano, M. The SCF ubiquitin ligase: insights into a molecular machine. *Nat. Rev.*
1192 *Mol. Cell Biol.* **5**, 739–751 (2004).
1193 69. Petroski, M. D. & Deshaies, R. J. Mechanism of Lysine 48-Linked Ubiquitin-Chain Synthesis by
1194 the Cullin-RING Ubiquitin-Ligase Complex SCF-Cdc34. *Cell* **123**, 1107–1120 (2005).
1195 70. Yu, Y., Dumollard, R., Rossbach, A., Lai, F. A. & Swann, K. Redistribution of mitochondria leads
1196 to bursts of ATP production during spontaneous mouse oocyte maturation. *J. Cell. Physiol.* **224**,
1197 672–680 (2010).
1198 71. Dalton, C. M. & Carroll, J. Biased inheritance of mitochondria during asymmetric cell division in
1199 the mouse oocyte. *J. Cell Sci.* **126**, 2955–2964 (2013).
1200 72. Rodríguez-Nuevo, A. *et al.* Oocytes maintain ROS-free mitochondrial metabolism by suppressing
1201 complex I. *Nature* **607**, 756–761 (2022).
1202 73. Sies, H., Berndt, C. & Jones, D. P. Oxidative Stress. *Annu. Rev. Biochem.* **86**, 715–748 (2017).
1203 74. Snow, A. J. *et al.* Phosphorylation-dependent interaction of tyrosine 3-monooxygenase/
1204 tryptophan 5-monooxygenase activation protein (YWHA) with PADI6 following oocyte maturation
1205 in mice. *Biol. Reprod.* **79**, 337–347 (2008).
1206 75. Rose, R., Rose, M. & Ottmann, C. Identification and structural characterization of two 14-3-3
1207 binding sites in the human peptidylarginine deiminase type VI. *J. Struct. Biol.* **180**, 65–72 (2012).
1208 76. Han, Z. *et al.* The subcortical maternal complex modulates the cell cycle during early mammalian
1209 embryogenesis via 14-3-3. *Nat. Commun.* **15**, 8887 (2024).
1210 77. Hanisch, A., Silljé, H. H. W. & Nigg, E. A. Timely anaphase onset requires a novel spindle and
1211 kinetochore complex comprising Ska1 and Ska2. *EMBO J.* **25**, 5504–5515 (2006).
1212 78. Welburn, J. P. I. *et al.* The Human Kinetochore Ska1 Complex Facilitates Microtubule
1213 Depolymerization-Coupled Motility. *Dev. Cell* **16**, 374–385 (2009).
1214 79. Jeyaprakash, A. A. *et al.* Structural and Functional Organization of the Ska Complex, a Key
1215 Component of the Kinetochore-Microtubule Interface. *Mol. Cell* **46**, 274–286 (2012).

1216 80. Neeli, I., Khan, S. N. & Radic, M. Histone Deimination As a Response to Inflammatory Stimuli in
1217 Neutrophils. *J. Immunol.* **180**, 1895–1902 (2008).
1218 81. Christophorou, M. A. *et al.* Citrullination regulates pluripotency and histone H1 binding to
1219 chromatin. *Nature* **507**, 104–108 (2014).
1220 82. Edgar, R. Gene Expression Omnibus: NCBI gene expression and hybridization array data
1221 repository. *Nucleic Acids Res.* **30**, 207–210 (2002).
1222 83. Perez-Riverol, Y. *et al.* The PRIDE database resources in 2022: a hub for mass spectrometry-
1223 based proteomics evidences. *Nucleic Acids Res.* **50**, D543–D552 (2022).
1224 84. Concordet, J.-P. & Haeussler, M. CRISPOR: intuitive guide selection for CRISPR/Cas9 genome
1225 editing experiments and screens. *Nucleic Acids Res.* **46**, W242–W245 (2018).
1226 85. Burgoyne, P. S., Mahadevaiah, S. K., Perry, J., Palmer, S. J. & Ashworth, A. The Y*
1227 rearrangement in mice: new insights into a perplexing PAR. *Cytogenet. Genome Res.* **80**, 37–40
1228 (1998).
1229 86. Earl, C. P. *et al.* Capture, mutual inhibition and release mechanism for aPKC–Par6 and its
1230 multisite polarity substrate Lgl. *Nat. Struct. Mol. Biol.* (2025) doi:10.1038/s41594-024-01425-0.
1231 87. Harshil Patel *et al.* nf-core/rnaseq: nf-core/rnaseq v3.18.0 - Lithium Lynx. Zenodo
1232 https://doi.org/10.5281/ZENODO.1400710 (2024).
1233 88. Wolf, F. A., Angerer, P. & Theis, F. J. SCANPY: large-scale single-cell gene expression data
1234 analysis. *Genome Biol.* **19**, 15 (2018).
1235 89. Huang, D. W., Sherman, B. T. & Lempicki, R. A. Systematic and integrative analysis of large
1236 gene lists using DAVID bioinformatics resources. *Nat. Protoc.* **4**, 44–57 (2009).
1237 90. Sherman, B. T. *et al.* DAVID: a web server for functional enrichment analysis and functional
1238 annotation of gene lists (2021 update). *Nucleic Acids Res.* **50**, W216–W221 (2022).
1239